The glycocalyx affects force loading-dependent mechanotransductive topography sensing at the nanoscale

[1]Matteo Chighizola[F], [1,2]Tania Dini, [3]Stefania Marcotti, [1,2,4]Mirko D'Urso, [1]Claudio Piazzoni, [1]Francesca Borghi, [1]Anita Previdi, [1]Laura Ceriani, [1,2]Claudia Folliero, [3]Brian Stramer, [1]Cristina Lenardi, [1]Paolo Milani, [1]Alessandro Podestà*, [1]Carsten Schulte*

Affiliations:

matteo.chighizola@unimi.it, claudio.piazzoni@unimi.it, francesca.borghi@unimi.it, anita.previdi@unimi.it, laura.ceriani3@studenti.unimi.it, follieroclaudia@gmail.com, cristina.lenardi@unimi.it, paolo.milani@mi.infn.it, alessandro.podesta@mi.infn.it, carsten.schulte@unimi.it

[1]Interdisciplinary Centre for Nanostructured Materials and Interfaces (C.I.Ma.I.Na.) and Department of Physics "Aldo Pontremoli", University of Milan, Milan, Italy

tania.dini@ifom.eu

[2]The FIRC Institute of Molecular Oncology (IFOM), Milan, Italy

stefania.marcotti@kcl.ac.uk, brian.m.stramer@kcl.ac.uk

[3]Randall Centre for Cell and Molecular Biophysics, King's College London, London, United Kingdom

m.d.urso@tue.nl

[4]Department of Biomedical Engineering, Institute for Complex Molecular Systems, Eindhoven University of Technology, Eindhoven, Netherlands

[F] first author

***Co-last and corresponding authors:**

Carsten Schulte: carsten.schulte@unimi.it

Alessandro Podestà: alessandro.podesta@mi.infn.it

Keywords:

Integrin adhesion complexes, glycocalyx, mechanotransduction, molecular clutch, focal adhesion, force loading, biophysics, nanotopography, biomaterials, Atomic Force Microscopy, force spectroscopy, colloidal probes

ABSTRACT

The cell/microenvironment interface is the starting point of integrin-mediated mechanotransduction, but many details of mechanotransductive signal integration remain elusive due to the complexity of the involved (extra)cellular structures, such as the glycocalyx.

We used engineered nano-bio interfaces with extracellular matrix nanotopography-mimicking features to analyse the impact of the glycocalyx on nano-mechanosensing. Our data demonstrates that the glycocalyx configuration affects spatiotemporal nanotopography-sensitive mechanotransductive events at the cell/microenvironment interface. Opposing effects of glycocalyx removal were observed, when comparing flat and specific nanotopographical conditions (*i.e.*, 15 nm root-mean-square (rms) roughness). In fact, the excessive force loading and retrograde actin flow speed, characteristic for the 15 nm rms nanotopography in the presence of native glycocalyx, are strongly reduced in its absence. Conversely, on the flat substrate, these parameters increased upon glycocalyx-targeting enzymatic treatment.

Our results highlight the importance of the glycocalyx configuration in a molecular clutch force loading-dependent cellular mechanism for nano-mechanosensing of the topography.

1. INTRODUCTION

In recent years, there has been accumulating evidence of the pivotal importance of integrin-mediated mechanosensing and mechanotransduction, *i.e.* the conversion of biophysical cues from the microenvironment into cellular responses, in virtually all cell biological contexts, particularly during cell migration and differentiation. At the base of mechanotransductive processes are the events at the interface between the cell and the extracellular matrix (ECM). At this site, the microenvironmental biophysical cues are translated into intracellular signals, with integrin adhesion complexes (IAC) as the major relay station. Linkages between the ECM and the actin cytoskeleton (f-actin) via integrin and talin, *i.e.* the formation of so-called molecular clutches, enable force transmission from the actin retrograde flow, which, in turn, is generated by actin polymerisation and the myosin-driven contraction of f-actin. These interfacial actions depend on the structural and biophysical ECM properties and regulate in an intricate manner the force loading within the molecular clutches, the maturation of IAC, their transformation into signalling platforms, and cytoskeletal remodelling, which together convert into cellular responses[1,2,3,4,5,6]. The involved (extra)cellular structures in this cell/microenvironment interface, such as the ECM, the glycocalyx, the cell membrane, the IAC and the cytoskeleton, are highly complex and their sophisticated crosstalk is only partially understood.

ECM nanotopography represents an important biophysical cue for mechanotransductive processes. The configuration of topographical nano-3D features determines spatial parameters relevant for mechanosensing, such as adhesion site areas and spacing, and is therefore capable of modulating IAC formation and signalling[6,7,8,9,10,11,12,13]. Moreover, the three-dimensionality of the surface topography introduces also further levels of complexity, compared to flat substrates[3,7,14,15,16] (Fig. 1A). Work by Park *et al.* revealed that the same nanotopographical features can provide different information to cells. The cellular cortical stiffness and the extent to which the cell can sufficiently deform in order to contact the intervening surface between topographical features will determine the effective cell/substrate contact area at the nanoscale[17,18]. Our previous work demonstrated that intrinsic cellular parameters, such as the availability of activated integrins, also regulate nanotopography mechanosensing and force loading[19].

An underappreciated player in mechanotransduction is the glycocalyx, a pericellular sugar coat that is attached to the cell surface. It is known that the glycocalyx can promote integrin clustering[2,20,21,22,23,24]. However, most studies in this context have been done on flat substrates and therefore many details remain elusive about the impact of the glycocalyx on the nanotopography-sensitive interfacial biophysics of molecular clutches and IAC formation, which was one of the main rationales behind this work.

In this framework, we use a bottom-up nanofabrication technique, called supersonic cluster beam deposition (SCBD)[25,26], to mimic ECM nanotopographies (assembled by clusters of zirconia nanoparticles). These nano-bio interfaces possess the potential to modulate mechanotransductive processes[9,10,13,26], as well as cellular functioning, programme and differentiation in various cell biological contexts[9,13,27,28,29,30]. Recently, we have furthermore developed an approach to test integrin-related nanoscale mechanotransductive processes, by means of atomic force microscopy (AFM)-based adhesion force spectroscopy measurements using custom nanostructured colloidal probes[19] (Fig. 1B).

Here, we exploited these nano-bio interfaces to dissect the role of the glycocalyx in spatiotemporal events that occur at the cell/microenvironment interface and during nanotopography mechanosensing (Fig. 1). In particular, we manipulated the nanotopographical features, the glycocalyx and ROCK-dependent actomyosin contractility to influence and analyse (by AFM-based adhesion force spectroscopy approaches) the consequent interfacial dynamics. Moreover, we studied the impact of the nanotopography and

glycocalyx on the molecular clutch engagement to the actin retrograde flow in lamellipodia by means of optical imaging techniques.

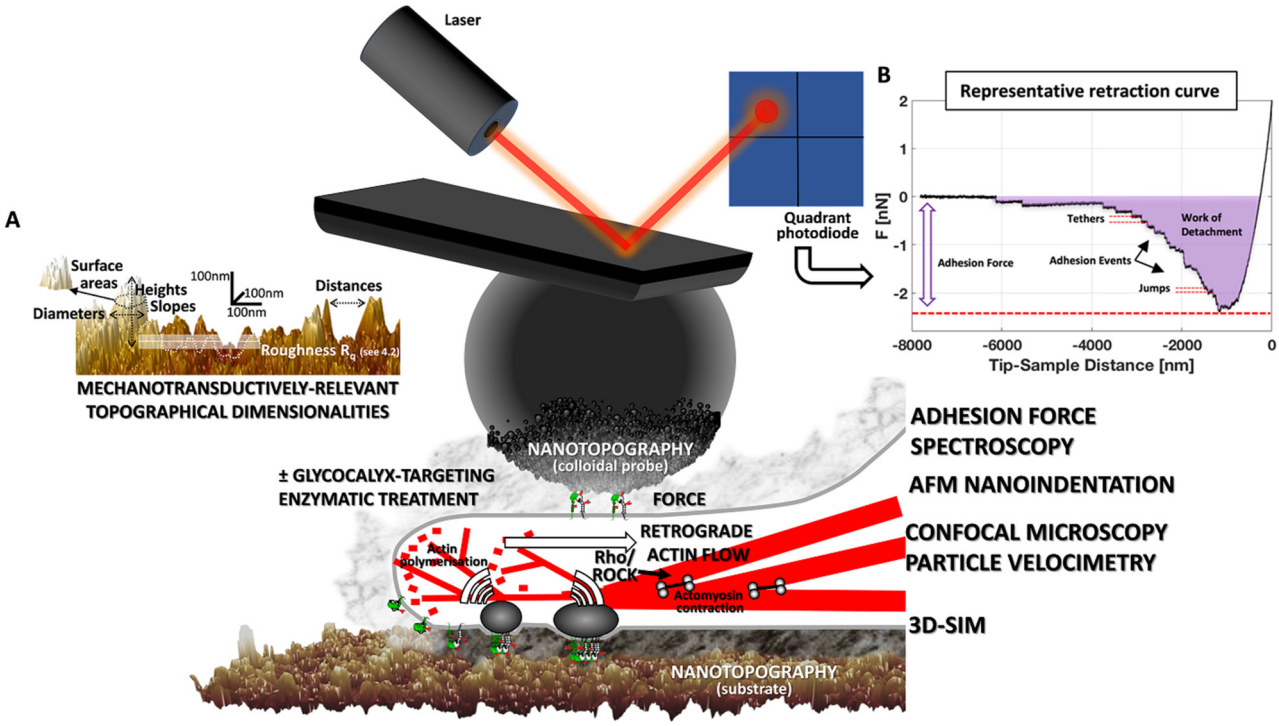

Fig. 1) Applied approaches to study the impact of the glycocalyx on force loading-dependent mechanotransductive topography sensing at the nanoscale. *The figure visualises the different mechanotransductive parameters (e.g., force loading and retrograde actin flow) and events at the cell/microenvironment interface that were scrutinised with the applied AFM- and optical imaging-based techniques (adhesion force spectroscopy, nanoindentation, particle velocimetry, 3D-SIM). In particular, we studied the involvement of the glycocalyx (by enzymatic treatment) in nanotopography-sensitive and molecular clutch force loading-dependent mechanotransductive processes. The ECM-mimicking nanotopographical surfaces (on colloidal probes for adhesion force spectroscopy or as cell substrates) were produced via zirconia cluster assembling by means of supersonic cluster beam deposition.* ***(A)*** *The graphic highlights in detail mechanotransductively-relevant topographical dimensionalities at the nanoscale, distinguished from flat 2D substrates, which we discuss throughout this work.* ***(B)*** *A representative retraction curve from the adhesion force spectroscopy measurements is shown, highlighting cell adhesion-related parameters extracted from them.*

2. RESULTS AND DISCUSSION

2.1 Structural assessment of the native PC12 cell glycocalyx

To understand how the glycocalyx participates in mechanosensing of nanotopographical features and how it influences interfacial mechanotransductive processes, we first determined the structural configuration of the native glycocalyx of PC12 cells. The neuronal-like PC12 cell model was selected due to our previous studies that demonstrated how nanotopographical features robustly modulate the mechanotransductive structures and signalling in these cells[9,10,19]. We furthermore assessed the efficiency of a comprehensive glycocalyx-targeting enzymatic treatment (an enzymatic cocktail of hyaluronidase II, chondroitinase ABC, heparinase III, and neuraminidase) by AFM- and 3D-SIM-based techniques (Fig. 2), to validate the possibility to manipulate the glycocalyx by this approach.

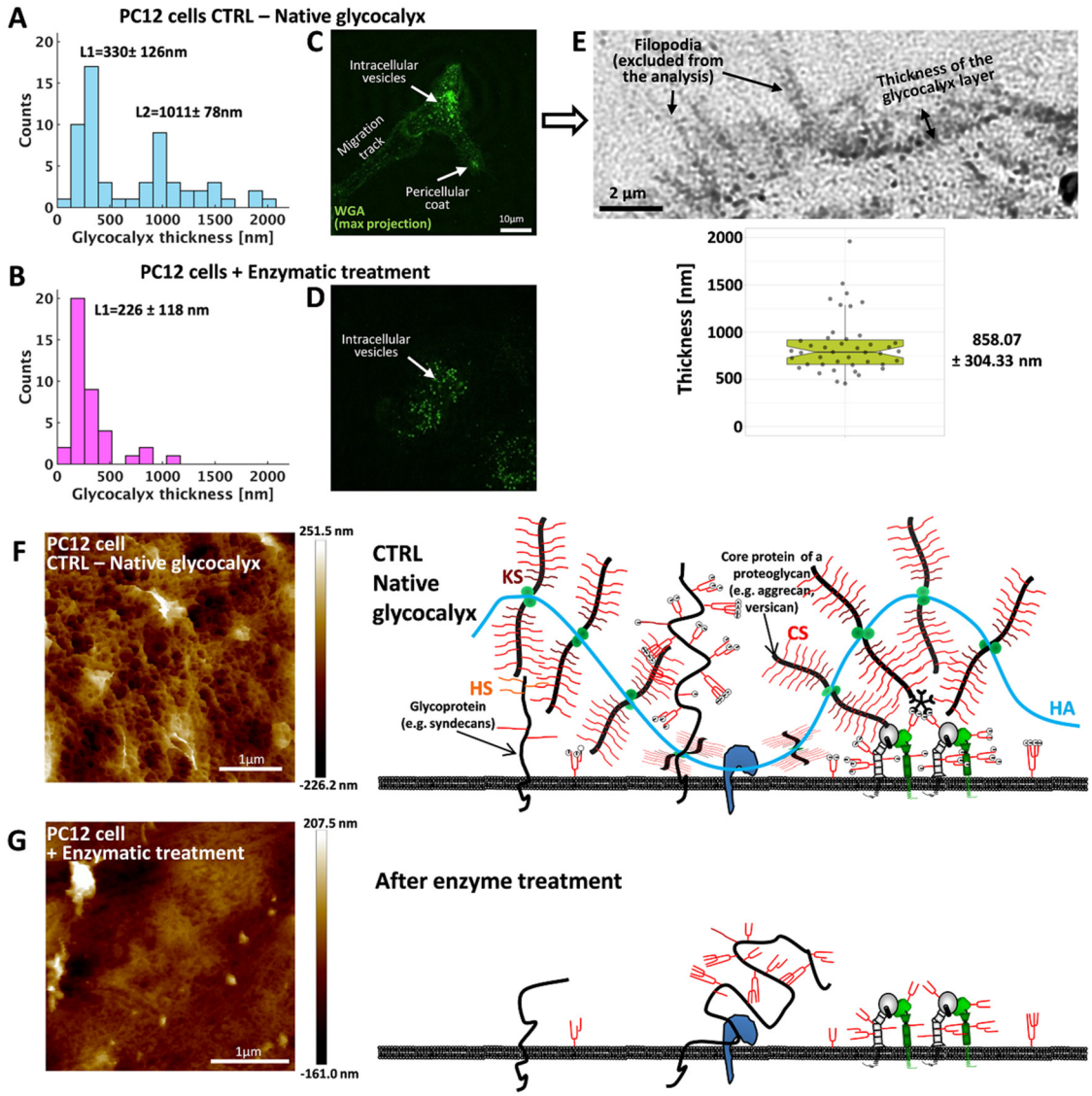

Fig. 2) Analyses of the glycocalyx configuration by AFM-based techniques and 3D-SIM imaging before and after treatment with a glycocalyx-targeting enzymatic cocktail. A,B) *Glycocalyx thickness (after an analysis following the Sokolov et al. protocol[31,32,33], further details can be found in SI1) derived from indentation measurements made on* ***A)*** *native PC12 cells or* ***B)*** *PC12 cells treated with a glycocalyx-targeting enzyme cocktail (containing hyaluronidase II, chondroitinase ABC, heparanase, and neuraminidase) on PLL. Each count corresponds to one cell.* ***C,D)*** *Representative 3D-SIM images (max. projection) of* ***C)*** *PC12 cells on PLL, native or* ***D)*** *treated with the glycocalyx-targeting enzymatic cocktail, marked with Oregon Green® 488 conjugated wheat germ agglutinin (WGA) which binds to sialic acid and N-acetylglucosaminyl residues.* ***C)*** *The image shows the native PC12 cells with different glycocalyx-containing (extra)cellular structures stained in green, i.e. intracellular vesicles filled with glycocalyx components, the pericellular glycocalyx coat (details in (E)) and a migration track/migrasome (a extracellular structure/organelle known to be left behind by some migrating cells[34,35,36]).* ***D)*** *After the enzymatic treatment all stainings disappeared, except for the intracellular vesicles.* ***(E)*** *Representative close-up of native PC12 cell marked with WGA (pixel intensities were inverted for clarity), from a plane just above the substrate used for the quantification of the thickness of the glycocalyx layer. The boxplot below shows the mean and 95% confidence intervals as box limits of the glycocalyx thickness analysis from 43 such close-up zones taken from 15 different images.* ***(F)*** *On the left, the appearance of native (fixed) PC12 cells covered with the glycocalyx in AFM peak force tapping is shown (upper image), compared to the situation after treatment with the glycocalyx-targeting enzymatic cocktail (bottom image). On the right, the according cartoons summarise and integrate the data obtained with the AFM- and 3D-SIM-based glycocalyx analyses and visualise*

schematically the glycocalyx configuration in its native state and after the enzymatic treatment. HS = Heparan-Sulphate, KS = Keratan-Sulphate, CS = Chondroitin-Sulphate, HA = Hyaluronic acid.

We performed AFM indentation experiments to test the mechanical and structural properties of the glycocalyx of live PC12 cells, based on the protocol developed by Sokolov *et al.*[31,32,33] (SI1 and SI - Fig. S1-3). The quantification of the control PC12 cells (Fig. 2A) demonstrated the presence of a long component of the native glycocalyx with a thickness of 1011 ± 78 nm and a short component with a thickness of 330 ± 126 nm (details on the Sokolov bilayer brush model and the long and short component can be found in SI1). The enzymatic digestion of the glycocalyx almost completely removed the long component of the glycosidic brush. Only in 10 % of the measured cells this long component was still present after the enzymatic treatment, and where it could still be found, it was significantly shorter (-21.4%) with a thickness of 795 ± 150 nm. The short component was still present, but also shortened by 31.5% to a thickness of 226 ± 118 nm (Fig. 2B).

3D-SIM super-resolution imaging of live PC12 cells (Fig. 2C-E) revealed the presence of abundant intracellular vesicles (through which glycocalyx components are presumably transported to the surface) and a clear pericellular sugar brush around the cells. We also detected migration tracks, extracellular structures/organelles left behind by many migrating cells[34,35,36]. The staining of the pericellular sugar coat and the migration tracks disappeared after enzymatic treatment, with only the intracellular vesicles remaining. A quantification of the thickness of this sugar coat at the border of the lamellipodial zones of the control cells revealed that it is 858.1 ± 304.3 nm thick, in good agreement with the values obtained by the AFM-based analysis.

Imaging of fixed PC12 cells (with or without enzymatic treatment) by AFM showed that the native cell surface was characterised by porous, reticular and filamentous structures (Fig. 2F), which became smooth after the enzymatic treatment with few remaining agglomerates (Fig. 2G).

Altogether, these analyses confirmed the presence of a substantial glycocalyx layer around native PC12 cells and the efficacy of the glycocalyx removal by the enzymatic treatment.

2.2 Nanoscale differences in the topography modulate the temporal adhesion and force loading dynamics

PC12 cells, in presence of their native glycocalyx, interact predominantly with the apical part of the asperities of zirconia cluster-assembled nanostructured surfaces (ns-Zr). Certain nanometric asperity parameters (Fig. 1A), such as apical surface area and peak to peak distances (mutable by changing the substrate roughness), oscillate around critical thresholds that are highly relevant for IAC formation. Spatial restrictions of the cellular adhesion site dimensions at the nanoscale (in the case of a roughness (see 4.2) parameter R_q = 15 nm, ns-Zr15) keep IAC at the focal complex size and diminish stress fibre development, compared to featureless, flat zirconia films (flat-Zr) on which the IAC mature to FA and stress fibres form[9]. Recently, we also showed, by adhesion force spectroscopy on PC12 cells using colloidal probes decorated with the ns-Zr15 surface, that during nascent adhesion formation these specific nanotopographical features can cause excessive force loading in integrin-mediated nanometric adhesion sites, leading to their disassembly, regulated by availability of activated integrins[19].

Here, we analysed how the adhesion and force loading dynamics towards different nanotopographical features change in the presence or absence of the glycocalyx (Fig. 3).

We therefore performed adhesion force spectroscopy on PC12 cells in the presence of native glycocalyx and after treatment with glycocalyx-targeting enzymes, using colloidal probes decorated with three different topographies (typical representations of the morphological features are shown in SI2 – SI Fig. S4): flat-Zr with a roughness parameter R_q <1 nm, ns-Zr15 (R_q = 15 nm), and ns-Zr20 (R_q = 20 nm); the latter two produced by SCBD (fabrication details in 4.1-2). The structure and morphology of the nanostructured films result from the random stacking and aggregation of impinging nanometric particles of ZrO_2. The surface morphology of the cluster-assembled zirconia films are characterised by distinct peaks and valleys (Fig. 1A), defining a complex random pattern of nanometric features, whose dimensions and spatial distribution resemble those found in natural ECM topographies (in particular in basement membranes)[3,7,14,15,16,37]. Various cell/probe contact times covering different stages of the critical window of nascent adhesion formation towards maturation to focal adhesions[38,39], *i.e.* 0 s, 20 s, 60 s, 120 s, and 240 s, were implemented.

From these measurements we derived information on the maximum adhesion force F_a (Fig. 3A), the work W (SI3 – SI Fig. S5A), the number of jumps N_j (Fig. 3B) and tethers N_t (SI3 – SI Fig. S5B), the mean jump force $\langle F_j \rangle$ (Fig. 3C), and the distribution of jump force (Fig. 3D). Jump events are usually associated to receptors in the membrane that are somehow anchored to the cytoskeleton, as for integrins engaged in molecular clutches[40,41,42,43], while the tether events are attributed to receptors that are not bound to the cytoskeleton[44,45]. We have shown previously that the jumps represent adhesion sites mediated, at least partially, by activated β1 subunit-containing integrins[19].

In the presence of the native glycocalyx (solid lines in Fig. 3), the results for flat-Zr and ns-Zr15 closely reproduced the outcome of our previous publication[19]. The maximum adhesion force F_a was generally low in the flat-Zr condition and N_j increased progressively until reaching a plateau. A different situation was found for the ns-Zr15 condition, where the F_a reached higher values and N_j fluctuated heavily, *i.e.* first increasing strongly at 20 s and then abruptly dropping towards at 60 s. This was reflected in a significant divergence of the $\langle F_j \rangle$ for the two conditions. Whereas this value had only minor variations in the flat-Zr condition, a rise to higher values in the ns-Zr15 condition with a maximum at 60 s was observed. Interestingly, the values for ns-Zr20 condition were instead akin to the flat-Zr condition, not to the ns-Zr15 condition. The values for W and N_t wavered around similar values in all three conditions (SI3 – SI Fig. S5, solid lines). A dissection of the jump force distribution (Fig. 3D) showed for flat-Zr that most jump forces were in the <50 pN category at all time points, with only a minor increase of intermediate (50-100 pN) and higher forces (>100 pN) over time. For ns-Zr15, there was instead an early shift (starting already at 20 s) towards the higher forces, *i.e.* >100 pN, even with appearance of some very high forces. The ns-Zr20 condition was intermediate, the jump force distribution was more equilibrated than in the other two conditions, with the 50-100 pN category being the predominant one for most time points (except 120 s).

These data show that differences in nanoscale topographical features can have a significant effect on important cellular adhesion parameters and interfacial force-related mechanotransductive processes at the cell membrane level.

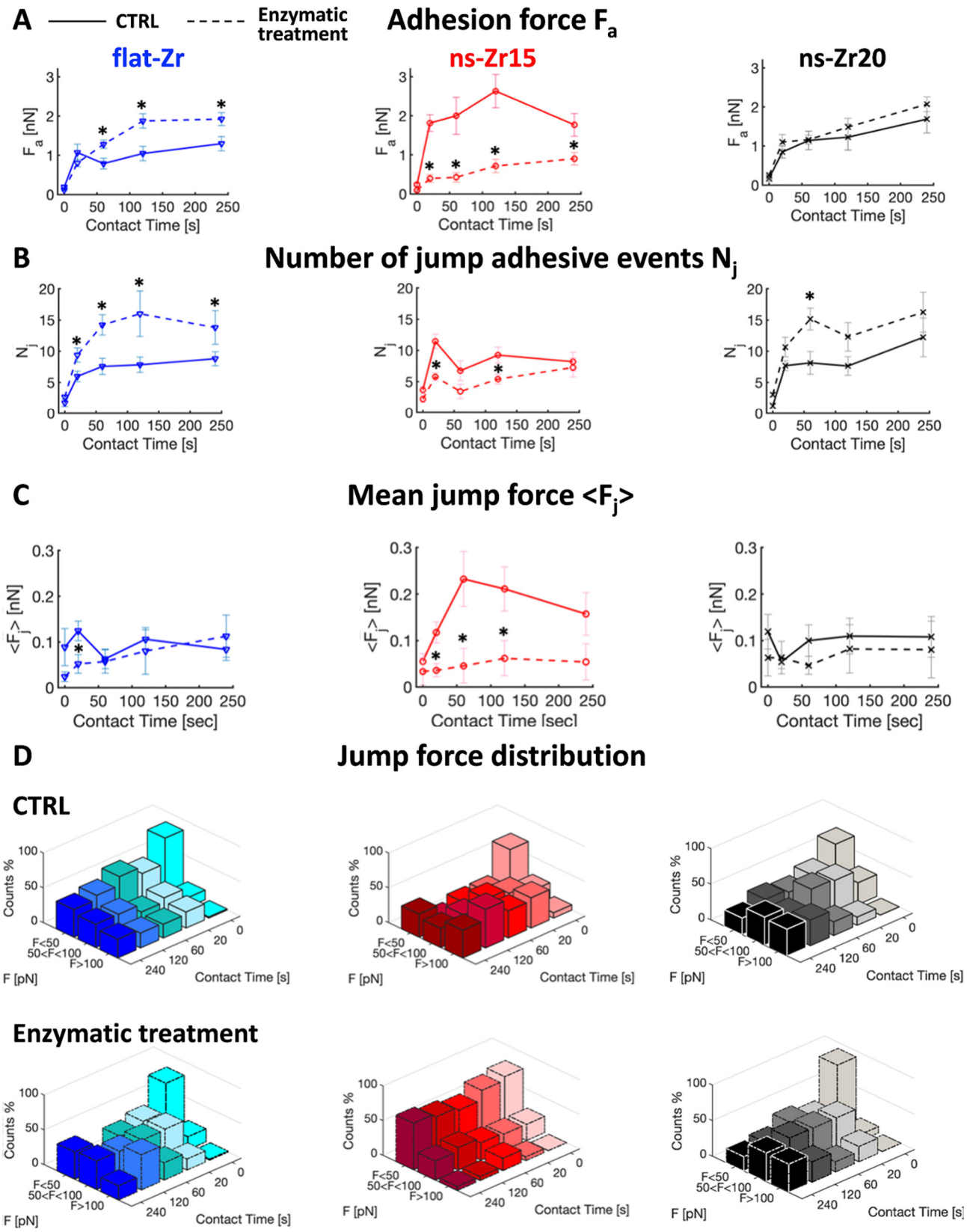

E

Table 1 – Most probable jump forces at 0 s

Topography/experimental condition	CTRL	Enzymatic treatment
flat-Zr	44 ± 16 pN	25 ± 18 pN
ns-Zr15	39 ± 16 pN	28 ± 10 pN
ns-Zr20	43 ± 17 pN	33 ± 11 pN

Fig. 3) Differences in the nanotopography can induce specific adhesion dynamics that strongly depend on the glycocalyx configuration. *The panel shows the results of the adhesion force spectroscopy measurements for probes with flat zirconia films devoid of nanotopographical features (flat-Zr, blue lines or bars), and with nanostructured ECM-mimicking cluster-assembled zirconia films with a roughness R_q of 15 nm rms (ns-Zr15, red lines or bars), or 20 nm rms (ns-Zr20, black lines or black/grey bars), in the presence of the cell's native glycocalyx (solid lines or bars), or after glycocalyx removal (dashed lines or bars with border lines). The measurements were taken at 5 different cell/probe contact times (0 s, 20 s, 60 s, 120 s, and 240 s). The parameters presented in this graph are* ***(A) Maximum adhesion force F_a, (B) Number of jump bonds N_j, and (C) Mean strength of jump bonds $<F_j>$*** *(Work W and Number of tether bonds N_t can be found in SI3 – SI Fig. S5). The error bars represent effective standard deviation of the mean details in 4.3.4). Asterisks indicate significant differences between control and glycocalyx-targeting enzymatic treatments.* ***(D)*** *The bars shows the temporal evolution of the jump force distributions (allocating the forces into 3 categories; i.e. low forces <50 pN, intermediate forces, 50-100 pN, high forces >100 pN (a finer binning can be found in the SI4 – SI Fig. S6, to see the dispersion of higher forces) for the different experimental conditions.* ***(E)*** *The table shows the most probable jump forces at 0 s for the different experimental conditions.*

2.3 The configuration of the glycocalyx impacts on the mechanosensing of the nanotopography

After glycocalyx-targeted enzymatic treatment, some interesting and divergent effects could be observed (dashed lines in Fig. 3 and SI3 – Fig. S5). For the ns-Zr15 condition, the enzymatic treatment had a strong impact on several parameters, it reduced F_a, N_j, $<F_j>$ and W to values that were actually very similar to those we observed for the flat-Zr condition with the native glycocalyx, or even below, from 20 s onwards. For the flat-Zr condition, the removal of the glycocalyx had instead the opposite effect for F_a and N_j, leading to increased values that are comparable to the ns-Zr15 situation with the native glycocalyx or even higher, whereas W and $<F_j>$ (except 120 s) remained basically unchanged. For ns-Zr20, the variations due to the glycocalyx-targeting enzymatic treatment were more modest, the W (for the 120 s and 240 s time points) and N_j (at 60 s) increased at certain time points, whereas F_a and $<F_j>$ did not alter. The removal of the glycocalyx had a drastic effect on the jump force distribution (Fig. 3D) in the ns-Zr15 condition, as the majority of the jump forces was found in the <50 pN category for all time points. A minor fraction of forces was in the 50-100 pN category, whereas higher forces were practically absent. This was an almost complete inversion compared to the untreated cells interacting with this nanotopographical surface. The glycocalyx-targeting treatment had instead little impact on the jump force distribution in the flat-Zr condition (slight shift to more intermediate forces) and there was almost no alteration for ns-Zr20 condition.

An interesting aspect was also observed with respect to the most probable jump forces at 0 s. The values for these first pristine interactions forming between integrins and substrate were reduced after glycocalyx removal in all topographical conditions (Fig. 3E - Table 1, see also SI4 – SI Fig. S6). This is congruent with the mechanical loading of integrins due to the adjacent compressed glycocalyx shown by Paszek *et al*.[21].

These results show that the glycocalyx has a decisive influence on the adhesion dynamics towards nanotopographical features and that this influence depends on the nanometric details of the topography, as evident especially for the case of ns-Zr15 (which has been shown to strongly modulate IAC-mediated mechanotransductive processes and signalling in PC12 cells[9,10,19]). Indeed, the impact of glycocalyx removal can strongly differ in dependency of the particular nanotopographical conditions. Overall, these data demonstrate a pivotal role of the glycocalyx in the cellular perception of the nanotopography, through the impact on force loading and distribution.

2.4 The glycocalyx configuration affects nanotopography-sensitive molecular clutch engagement to the retrograde actin flow

The forces that drive the force loading within molecular clutches derive from the retrograde actin flow, which, in turn, is generated by actin polymerisation and actomyosin contraction, regulated by Rho/ROCK signalling[1,2,5,6,46,47,48,49,50,51,52,53,54]. An inverse relationship between actin retrograde flow velocity and the traction forces has been demonstrated during transition from nascent adhesion to FA, *i.e.* IAC maturation causes actin flow deceleration by molecular clutch engagement and reinforcement[48,49,50,52]. For flat substrates, it is known that the initial integrin clustering in nascent adhesions is independent of actomyosin-driven forces[48,55] (and substrate mechanics[56]). The force loading in molecular clutches, IAC growth to FA, and stress fibre formation instead strongly depend on actomyosin contraction.

To understand how the interplay between microenvironmental nanotopography and the glycocalyx configuration modulates the retrograde actin flow speed (and accordingly the extent of molecular clutch engagement), we recorded the actin cytoskeletal dynamics (visualised by LifeAct™ transfection) of PC12 cells that interact with flat-Zr or ns-Zr15 substrates in the presence or absence of the glycocalyx.

Particle image velocimetry (Fig. 4A) demonstrated that the lamellipodial actin flow dynamics were significantly faster in the cells plated on ns-Zr15, compared to flat-Zr. This is in good accordance with the fact that on ns-Zr15 the IAC have focal complex dimension due to the nanotopography-imposed spatial restriction for integrin nanocluster formation, whereas there is focal adhesion formation on flat-Zr[9]. This nanotopography-dependent difference in actin flow speed equals when the cells were treated with the glycocalyx-targeting enzymes, meaning that the actin flow speed increased on flat-Zr and decreased on ns-Zr15.

Force spectroscopy measurements with the ns-Zr15 probes on PC12 cells treated with the ROCK inhibitor Y27632 revealed a clear change of the adhesion dynamics and forces with respect to the untreated cells (Fig. 4B). Differently from the ns-Zr15 of untreated cells, after Y27632 treatment N_j progressively increased over time, reaching particularly high levels at 120 s and 240 s. Compared to the untreated ns-Zr15 condition, a decrease in N_j at 20 s and an increase at later time points (in particular at 240 s) was observed and $\langle F_j \rangle$ was strongly reduced for the time points in the critical nascent adhesion formation window (20 – 120 s), with appearance of much less high forces. Also the most probable jump force at 0 s was reduced (25 ± 14 pN, compare to value of untreated cells in Fig. 3E, Table 1, *i.e.* 39 ± 16 pN).

These data demonstrate that molecular clutch engagement is nanotopography-sensitive in a glycocalyx-dependent manner and that the nanotopography mechanosensing relies on Rho/ROCK signalling-regulated actomyosin contraction. Notably, the contrary effect of the glycocalyx removal between flat-Zr and ns-Zr15 regarding the retrograde actin flow is congruent to what was seen regarding the adhesion force dynamics. Altogether, this confirms the importance of the glycocalyx and force-related processes for nanotopography sensing.

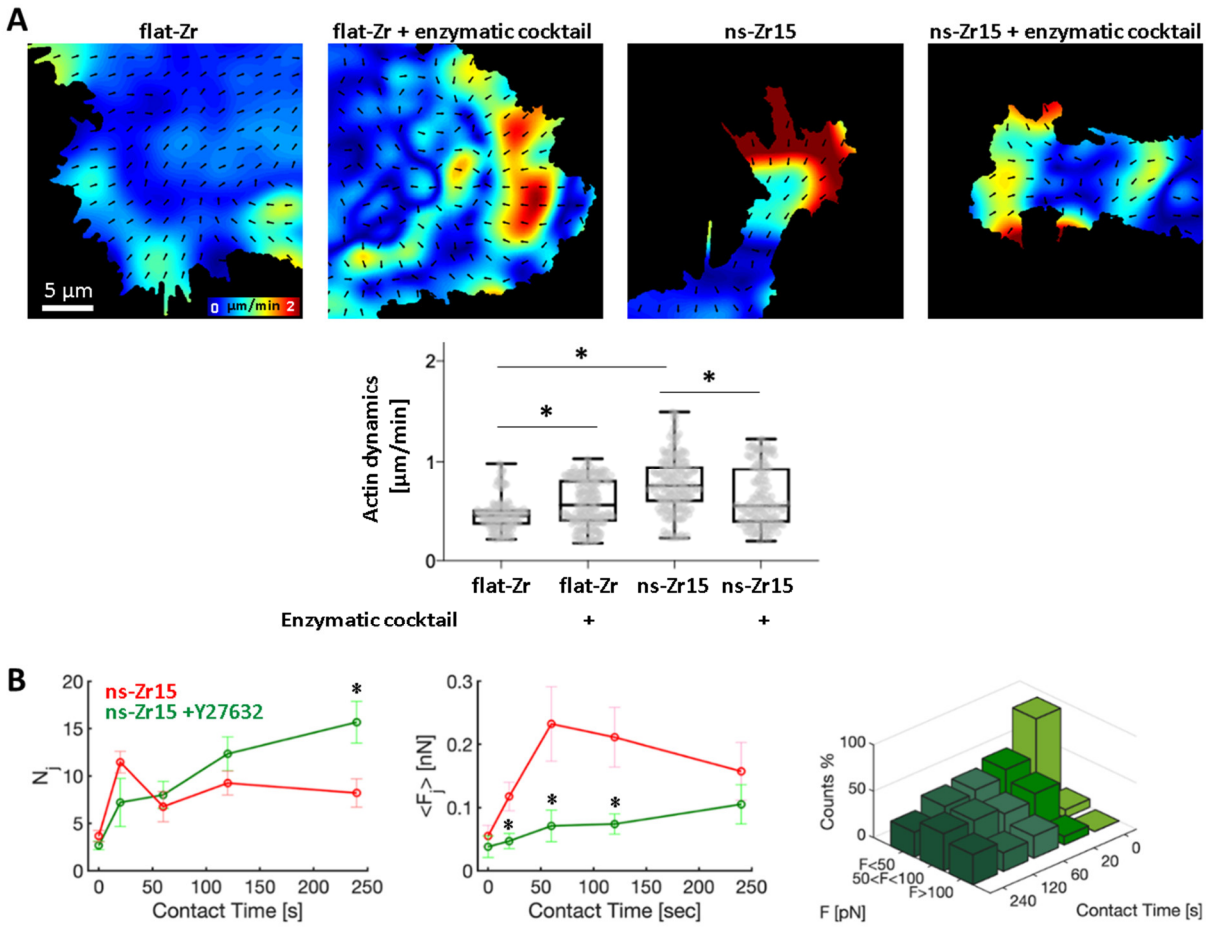

Fig. 4) The nanotopography and the glycocalyx configuration affect the lamellipodial molecular clutch engagement and actin dynamics. (A) *The panel shows representative actin flowfield images obtained after Particle Image Velocimetry (PIV) of live cell recordings of PC12 cells (transfected previously with LifeAct™-mCherry to visualise the actin dynamics) in the different indicated experimental conditions. The confocal recordings had a frame rate of 0.5 images/sec. The graph below shows the according PIV-based quantification of the actin dynamics. The boxplots show medians, 25th and 75th percentile as box limits. 198-234 frames from 11-14 cells/lamelllipodial zones were quantified. A Kruskal-Wallis statistical test with multiple comparisons of all possible sample permutations was applied. *P<0.05.* ***(B)*** *The graphs summarise the evolution of N_j, $<F_j>$ and jump force distribution comparing untreated PC12 cells interacting with ns-Zr15 (red lines, reproduced from Fig. 3B,C), or treated the ROCK inhibitor Y27632 (10 µM, green lines or bars, for ns-Zr15 CTRL jump force distribution, compare with Fig. 3D). The error bars represent effective standard deviation of the mean (details in 4.3.4).*

For flat-Zr, the effects of the glycocalyx removal (in particular the increase of N_j and actin retrograde flow speed, together with the decrease in initial jump force) are in good accordance with the paradigm established by Paszek *et al.*[21] (reviewed by Kechagia *et al.*[2]). A bulky glycocalyx promotes integrin clustering by funnelling of active integrins to an initial integrin/ligand binding site ("kinetic trap") and by applying additional tension due to upward force caused by the adjacent glycocalyx compression. The increase in the actin retrograde flow speed after glycocalyx removal indicates that abolition of these glycocalyx-dependent effects reduces the molecular clutch engagement and integrin clustering on the flat substrate.

Nanotopographical features apparently add another level of complexity (Fig. 1A) leading to particular glycocalyx-sensitive phenomena that are subject to the exact topographical configuration, as they are specific for the ns-Zr15 condition (the decrease in F_D, W, N_j, $<F_j>$, high force occurrence, and actin

retrograde flow speed). Previous characterisations of the nanotopographical asperities produced by SCBD[9] have shown the significance of their dimensionalities for mechanotransductive processes. The dimensions of the asperity features and the distances between them fluctuate around values determined to have high relevance for nascent adhesion growth and maturation (Fig. 1A), *i.e.* the modular nanometric integrin cluster size (50 – 100 nm diameter)[39,56], the minimal adhesion area and ligand geometry necessary for integrin clustering (> hundreds of nm^2, at least 4 ligands in tens of nm vicinity)[57,58,59,60], and the ligand spacing thresholds (around 60 nm)[61,62,63]. The difference between nanotopography roughness R_q 15 nm versus 20 nm has thus the potential to shift the adhesion site dimensionalities in a way that is significant for mechanotransductive processes in the cell/microenvironment interface. This holds in particular true taking into account the disorder of our nanostructured substrates because integrin clustering depends on the local arrangement of adhesion sites at the nanoscale rather than on the global average ligand density[64]. Interestingly, the range of dimensionalities of these nanotopographies closely resemble *e.g.* those found in different basement membranes[16].

In the presence of the native glycocalyx, the initial nascent adhesion formation, which is independent of actomyosin contraction, seems to be promoted in the ns-Zr15 condition (high N_j towards 20 s). However, the excessive force loading-dependent events (increase of $<F_j>$ and drop of N_j, which are dependent on actomyosin contraction) lead eventually to a lower molecular clutch engagement to the retrograde actin flow (higher speed compared to the flat-Zr condition). Concordantly, we know from our previous work that the IAC are of much smaller nanometric dimensions (focal complex size) on ns-Zr15 compared to the micrometric FA on flat-Zr[9]. The deceleration of the retrograde actin flow speed, after glycocalyx removal, insinuates instead an increased molecular clutch engagement compared to control ns-Zr15 condition. Easier membrane bending around the asperities enabled by glycocalyx removal has the potential to increase the accessible surface contact area, by the impact on deformability of the membrane[17] due to the omission of the repulsive forces of the compressed glycocalyx[2,21] (Fig. 1A and Fig. 5), an aspect that we will address in detail in future investigations. However, the differences between ROCK inhibition and glycocalyx removal for the ns-Zr15 situation, especially regarding the number of jumps (compare Fig. 3B and Fig. 4B), indicate a complex contribution of the glycocalyx configuration in nanotopography sensing.

Very recently, Di Cio *et al.*[65] found dysregulated actin dynamics (in epithelial cells) on nanopatterned substrates (assembled by electrospun nanofibers with width diameters of several hundreds of nm, the smallest size studied was 250 nm) which led to a disruption of the mechanically instable actin network collapsing into foci, *i.e.* contractile myosin rings. They saw furthermore that β1-integrin expressing cells were less sensitive to the fibre dimension than β3-integrin expressing cells. They propose therefore an actin architecture-dependent long-range, rather than a FA-dependent, mechanism for nanotopography sensing. Similar to our results, in their experiments the cells became insensitive to the nanofibre width upon ROCK inhibition.

Differently to Di Cio *et al.*, we here propose a molecular clutch force loading-dependent mechanism for nanotopography sensing, with a decisive involvement of the glycocalyx. The effect of the ROCK inhibition on the nanotopography sensing (through its impact on the force loading), *i.e.* that the cells become blind for the nanotopographical differences, has some similarities to the role of actomyosin contraction (by sarcomere-like contractile units) and force production in the rigidity sensing mechanism described by Wolfenson *et al.*[66,67]. They have shown that the rigidity sensing occurs by actomyosin-driven stepwise contractions (low nm steps with a frequency of 2-3 steps/sec). These contractions in themselves are independent of the substrate rigidity and non-mechanosensitive[68], but a force threshold of around 20-

25 pN has to be reached to enable IAC reinforcement[66]. Interestingly, the most probable jump forces we measured are in this range and are influenced by the glycocalyx (Fig. 3E, Table 1).

Albeit the substrates we used here are rigid, we have shown that these nanotopographies can directly affect the extent of integrin clustering and the IAC size at the nanoscale[9], as well as the force loading in molecular clutches[19]. On ns-Zr15, the effects on mechanotransduction actually resemble what can be observed on soft substrates[1,2,46,56]. Considering the work of Oria *et al.*[47] that points out the importance of the force loading in molecular clutches for spatial ligand sensing, the rigidity and nanotopography mechanosensing are likely to be interdependent. It can be speculated that, upon modulation of the substrate rigidity or nanotopography, also respective specific spatial and force-related threshold parameters will mutually shift, depending on their influence on the molecular clutch force levels. In addition, Changede *et al.*[60] found that nanocluster bridges of unligated integrins can form between adjacent (tens of nm) nanometric adhesion sites (mimicking ECM fibres) which alone are not sufficient to sustain IAC maturation. Our data strongly indicate that you also have to take into account the glycocalyx configuration and the nanotopography, as alterations therein can again change the whole setting in the cell/microenvironment interface.

The dynamic biophysical cue-dependent events in the cell/microenvironment interface exhibit an intriguing complexity. Understanding the mentioned interdependencies in more detail will be a challenging and very interesting field for future investigations and it is of high biomedical relevance, in particular with respect to cancer cell biology[18,22,24,67,69,70,71].

3. CONCLUSIONS

Our results much accord with the title of a review by Gasiorowski *et al.* "Biophysical cues and cell behaviour: The big impact of little things"[14], and shed some light on how the glycocalyx affects the cellular perception of nanotopographical features and impacts mechanotransductive events at the nanoscale.

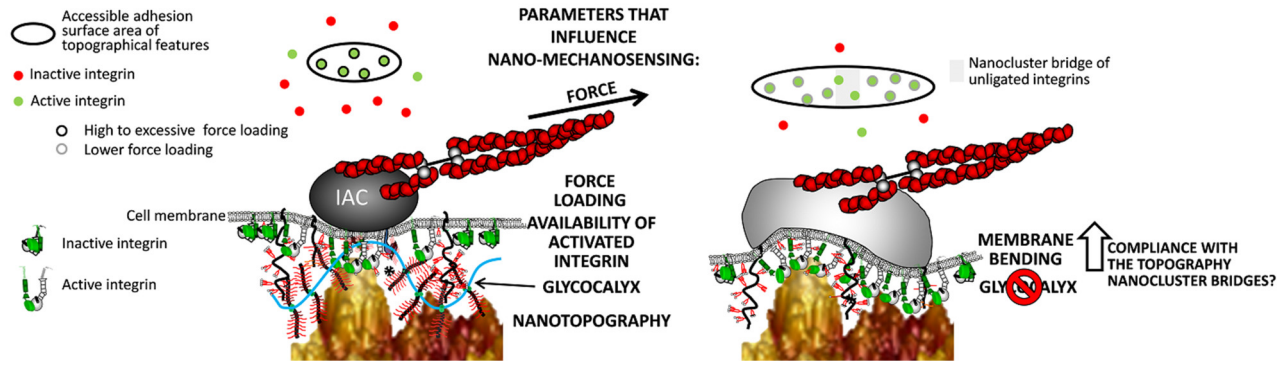

Fig. 5) Model for the way the glycocalyx affects force loading-dependent mechanosening of the nanotopography. *The figure summarises graphically the results of this work and visualises our model of the way the glycocalyx configuration might modulate the cellular perception of nanotopographical features the cells interacts with (based on our results and data published by others that we discuss). The presence or absence of the glycocalyx has the potential to influence the membrane bending and compliance with the nanotopography which changes the surface area of the asperities that is accessible for integrin adhesion complexes. This alters the integrin clustering and the force distribution/loading within the molecular clutches of nascent adhesions (for further details, see discussion above and conclusions).*

Altogether, our data clearly demonstrate that the glycocalyx, in a nanotopography-dependent manner, modulates decisively the dynamics of cellular adhesive and mechanotransductive processes,

particularly in regard to the number and structuring of adhesion sites at the nanometric scale and the force distribution within them. We show that the nanotopography and glycocalyx represent crucial factors within the cell/microenvironment interface that have to be considered in mechanotransduction in an interdependent manner. The configuration of the glycocalyx and further intrinsic cellular parameters, such as the type and availability of activated integrins (as we have shown in our previous work[19]) and the extent of engagement to actomyosin-driven forces, control how a cell actually perceives the nanotopographical features it interacts with. We have demonstrated for PC12 cells how manipulations of the glycocalyx, integrin activation and actomyosin contraction change the topography mechanosensing at the nanoscale. As a function of these intrinsic cellular factors, the same nanotopography can convey diverse cues to the cell (Fig. 5).

It can be speculated that these general mechanisms in the cell/microenvironment interface might be similar for many cell types. Particular adhesion and force loading dynamics towards nanotopographies will certainly differ, depending on the cell type-specific glycocalyx thickness and composition, integrin expression levels, integrin trafficking, the contractile machinery, cytoskeletal organisation and mechanics. One of our future objectives will be to dissect such differences (or find similarities in patterns) between cell types, and/or between healthy and pathophysiological situations. We have shown the capacity of our approach to detect even subtle meaningful differences in nanoscale mechanotransductive events.

The potential implications of these cell/microenvironment interfacial processes for pathophysiological situations become evident from the fact that aberrations in the components along the mechanotransductive sequence have been associated to various diseases[72], particularly to cancer and metastasis, as well as neurodegenerative diseases[22,69,70,71,73,74]. Examples are abnormal rearrangements and composition of the ECM[75,76,77] and glycocalyx[78], as well as dysregulation in IAC-related genes[79,80], or in the contractile machinery[71]. Recently, it has been shown that a glycocalyx-dependent potentiation of an integrin-mediated mechanosignalling feedback loop might be causally involved in the primary brain cancer glioblastoma multiple[81].

Here we concentrated on direct integrin-mediated mechanotransduction, but these results could have also broader relevance in the context of other transmembrane surface receptors; *e.g.* in syndecan-4/f-actin/integrin mechanotransductive crosstalk[82], during the clustering of receptors in synaptic perineuronal nets[83], or in CD44-mediated pericellular barriers (intracellular: cortical f-actin, extracellular: hyaluronic acid) that regulate receptor clustering (picket/fence model)[84]. Moreover, we have previously shown that other surface receptors, such as uPAR, can induce integrin activation and molecular clutch engagement by membrane tension-related processes[52,85]. Another aspect that might have an impact on these dynamics is the actin reorganisation that can be induced by nanotopography-dependent membrane bending (through curvature-sensing proteins, such as FBP17)[86].

Obtaining a deeper understanding of the mechanotransductive events in the cell/microenvironment interface at the nanoscale is thus essential and furthermore highly attractive from a biomedical, diagnostic and therapeutic perspective because the cellular outside and surface are easier to access than intracellular processes. This manifests in a recent re-evaluation and emergence of interest in potential ECM- and integrin-targeting drugs, or more general, so-called mechanotherapeutics[73,77,87,88].

4. MATERIALS AND METHODS

4.1 Fabrication and calibration of the colloidal probes

The procedure for the fabrication of colloidal probes (CP) is based on the approach described elsewhere[89,90]. The most important highlights of the protocol and the advantages of the probes that can be produced are reported below.

A borosilicate glass sphere (Thermo fisher Scientific), with nominal radii R = 5 μm for nanoindentation (see 4.3.3) and R = 10 μm for adhesion spectroscopy (see 4.3.1), is attached to a tipless silicon cantilever (Micromash HQ:CSC38/tipless/no Al, force constant *k* = 0.02 - 0.03 N/m) exploiting capillary adhesive forces or a small amount of vaseline as temporary adhesive. The glass sphere is then covalently attached to the silicon cantilever by thermal annealing for two hours in a high-temperature oven at the softening point temperature (T=780 °C). The resulting monolithic colloidal probe can be washed/cleaned aggressively after use in order to remove contaminants. The characterisation of the CP radius is performed by atomic force microscopy (AFM) reverse imaging of the probe on a spiked grating (TGT1, Tips Nano), as detailed in Indrieri *et al.*[89]. The spring constant is calibrated using the thermal noise method[91,92] where special correction factors are applied in order to take into account the relevant dimension and mass of the glass sphere[90,93].

4.2 Production of nanotopographical probes and substrates

For the production of the nanotopographical CPs (for adhesion force spectroscopy) and for the nanostructured substrates (for the retrograde actin flow experiments), ns-ZrO_2 films are deposited on the colloidal probes, or glass substrates, respectively, exploiting the SCBD technique (described in detail in the Ref.s[25,94,95]). Briefly, SCBD allows the production of nanostructured surfaces characterised by a disordered topography, yet with accurately controllable and reproducible morphological properties such as rms roughness, cluster size distribution and porosity[96,97,98]. Partially oxidised zirconia clusters are produced within the cluster source and then extracted into the vacuum of the expansion chamber through a nozzle to form a seeded supersonic beam. Clusters are collected directly on the CPs, or glass substrates, intercepting the beam in the expansion chamber. Upon landing on the sample surfaces, clusters form a nanostructured, highly porous, high-specific area, biocompatible ns-ZrO_2 film[26,29]. The protocol for the functionalisation of the colloidal probes with the nanotopographical surfaces achieved by zirconia cluster-assembling is detailed in Chighizola *et al.*[19]. The specific surface area, the rms roughness (defined as the standard deviation of the height of the surface, $r_q = \sqrt{\frac{1}{N}\sum_i (h_i - \bar{h})}$, where h_i is the height of the surface in a specific point, N is the number of pixels of the map and $\bar{h}$ is the average height), the average lateral dimensions of the largest morphological features (the correlation length ξ) typically increase with ZrO_2 film thickness[96,98,99].

4.3 AFM experiments

All the AFM experiments have been performed using a Bioscope Catalyst AFM (Bruker), mounted on top of an inverted optical microscope (Olympus X71). Isolation of the system from noise was obtained by means of both, an active anti-vibration base (DVIA-T45, Daeil Systems), and an acoustic enclosure for the AFM (Schaefer, Italy). During the AFM measurements performed on live cells, the temperature of the cell culture medium was maintained at 37°C using a perfusion stage incubator (PSI, Bruker) and a temperature controller (Lakeshore 331, Ohio, USA). Before every measurement the deflection sensitivity was calibrated *in situ* and non-invasively by using the previously characterised spring constant as a reference, according to the SNAP procedure described in Schillers *et al.*[100] and based on the assumption that the correct deflection sensitivity value must provide, through the noise calibration, the reference value of the spring constant. The cell regions to be investigated (portion of the membrane to be scanned or location of the force curves to be acquired) were chosen by means of the optical microscope; the accurate alignment of the optical and

AFM microscopes was obtained using the Miro (Bruker) module integrated in the AFM software. Data processing of the sets of curves and scan images was carried out in Matlab (Mathworks) environment using custom routines.

4.3.1 Adhesion force spectroscopy and data analysis

Adhesion force spectroscopy measurements were performed as discussed in detail in Chighizola *et al.*[19]. The nanotopographical colloidal probes (R= 10 μm) were incubated with the cell culture medium (Ø phenol red) for >30 min at 37°C before the actual measurements (to guarantee absorption of ECM proteins, such as fibronectin and vitronectin, present in the serum to the probes). Sets of force-distance curves were acquired at locations on the cells' body selected by means of the optical microscope. Force curves (FCs) containing 8192 points each were recorded on live PC12 cells, with ramp length l = 10 μm, maximum load F_{max} = 1 nN and retraction speed at v_r = 16 μm/s. The pulling speed was kept relatively low to reduce hydrodynamics effects[101]. To measure the early steps of cellular adhesion in the critical phase of nascent adhesion formation towards FA maturation, we selected five contact times (*cts*): 0, 20, 60, 120, 240 s, accordingly. During the contact time, the Z-piezo position was kept constant using the Z closed-loop feedback mode. The data analysis of the retraction curves was carried out using the protocol presented in Chighizola *et al.*[19].

4.3.2 Morphological characterisation of the glycocalyx operated in Peak-Force Tapping mode

The PC12 cells were fixed with 2% paraformaldehyde/0.1% glutaraldehyde in PBS for 30 min after 1 day of culturing on poly-L-lysine (PLL)-coated (0.1% w/v PLL solution (Sigma) for 30 min at RT) glass-bottomed plates (Willco Wells). The cell membrane morphology was characterised using a Bioscope Catalyst AFM from Bruker. The AFM images (with scan size of 3-5 μm) were acquired in PBS buffer in peak-force tapping mode. Because of the significant height variations within the samples (up to several micrometers), cantilevers with a tip height of 14 μm were used (VistaProbes CS-10). The scan rate was set to 0.6 Hz, the ramp frequency at 1 KHz, and the sampling resolution was set to 4096 × 1024 points. To avoid degradation of the glycocalyx, the measurements were performed within max. 24 hours following the fixation.

4.3.3 Glycocalyx characterisation by AFM nanoindentation

Nanomechanical indentation experiments were performed using colloidal probes with radius R = 5 μm following the approach presented by Puricelli *et al.*[102]. To get quantitative information about the thickness of the glycocalyx, the brush model was implemented by Sokolov *et al.*[31,32]. This model was developed with the purpose to decouple the single mechanical contributions of the glycocalyx compression and the underlying cell deformation, allowing isolating the force needed to compress the glycocalyx (for details, see SI2 and SI – Fig. S1-3).

4.3.4 Statistics and error analyses

For each observable ψ_{FCs} extracted by each force curve (FC) a mean value ψ_{cell} was evaluated for each cell. The error σ_{cell} associated to ψ_{cell} was obtained by summing in quadrature the standard deviation of the mean σ_{ψ} of the results coming from the single FCs and an estimated instrumental error $\sigma_{instrum}$ ($\sigma_{instrum} / \psi$ = 3%)[102].

$$\psi_{cell} = \frac{\sum_i^n \psi_{FCs}}{n}$$

where *n* is the number of force curves per each cell,

$$\sigma_{cell} = \sqrt{\sigma_{\psi}^2 + \sigma_{instrum}^2}$$

The final mean value ψ_{mean} representative of the cell population behaviour in a given condition was evaluated as:

$$\psi_{mean} = \frac{\sum_i^n \psi_{cell}}{N}$$

where *N* is the number of cells investigated for the given condition.

The final error σ_{mean} associated to ψ_{mean} was calculated by summing in quadrature the propagated error of the mean σ_s and the standard deviation of the mean of the singles cell values ψ_{cell}:

$$\sigma_{\mathrm{mean}} = \sqrt{\sigma_{\mathrm{std}}^2 + \sigma_{\mathrm{s}}^2}$$

where

$$\sigma_{\mathrm{s}} = \frac{1}{N}\sqrt{\sum_i \sigma_{cell}^2}\,,\ \sigma_{std} = \sqrt{\frac{\sum_i^n (\psi_{cell,i} - \psi_{fin})^2}{N}}$$

4.4 Cell culture and preparations for experiments

The experiments were performed with the neuron-like PC12 cells (PC12-Adh clone, ATCC catalogue no. CRL-1721.1TM). This cell line has shown to respond to the nanotopographical cues provided by the substrates produced by SCBD (in particular ns-Zr15) by mechanotransductive processes and signalling, which we have profoundly characterised in previous studies[9,10,19].

For routine cell culture (subculturing every 2-3 days using trypsin/EDTA solution), the PC12 cells were maintained (in a humid atmosphere at 37°C and 5% CO_2) in an incubator (Galaxy S, RS Biotech) provided with RPMI-1640 medium (supplemented with 10% horse serum, 5% fetal bovine serum, 2 mM 1-glutamine, 10 mM HEPES, 100 units mL^{-1} penicillin, 100 µg mL^{-1} streptomycin, 1 mM pyruvic acid). All reagents and materials from Sigma, also in the following, if not stated otherwise.

For the experiments, the cell detachment was done on the day before with an EDTA (1mM in PBS) solution to not digest the protein component of the glycocalyx. The cells were counted with an improved Neubauer chamber before plating them in a low concentration (4000 cells per cm^2, to have mostly single, separated cells) on the indicated substrates. The cells were then maintained in the incubator overnight to guarantee good cell adhesion.

For the experiments involving AFM measurements, the cells were seeded the day before the experiment on Ø 40 mm glass-bottomed plates (Willco Wells) that were coated before with PLL (0.1% w/v PLL solution for 30 min at RT). Solutions without phenol red were used, as it results harmful for the AFM tip holder.

For the actin dynamics measurements, one day before the experiment the cells (after LifeAct™ transfection, see 4.6.1) were instead plated on Ø 35 mm glass-bottomed dishes (MatTek, the Ø 13 mm glass was in the centre of the plate) on which either flat zirconia film (produced by ion gun sputtering) or nanostructured cluster-assembled zirconia film (fabricated by SCBD) have been deposited.

In case of glycocalyx-targeting enzymatic treatment, an enzyme cocktail was applied to the cell culture medium to obtain a final concentration of 13.5 U/mL hyaluronidase II, 150 mU/mL chondroitinase ABC, 300 mU/mL heparinise III and 150 mU/mL neuraminidase (these concentrations were inspired by the work of Zeng et al.[103]). The cells were incubated with these enzymes for 2 hours right before the experiments. Following the incubation, the cell culture medium was discarded. After washing 3x with PBS (to remove the digested glycocalyx), fresh medium was added containing again the enzymatic cocktail to avoid reassembly of the glycocalyx during the measurements.
For the Y27632 inhibition against ROCK, the cells were pre-incubated with the inhibitor 15 min before the measurements. The inhibitor was used at a final concentration of 10 µM.

4.5 Glycocalyx characterisation by wheat germ agglutinin staining and 3D-SIM

The glycocalyx of live PC12 cells in the indicated experimental conditions (prepared as described in 4.4) was marked 30 min before the recording by adding Oregon Green™ 488 conjugate wheat germ agglutinin (WGA, Thermofisher) to the medium at a final concentration of 25 µM/mL. WGA binds sialic acid and N-acetylglucosaminyl residues. After the 30 min incubation (in the incubator at 37°C and 5% CO_2), the cells were washed 3x with PBS to remove the excess of WGA (to reduce the background fluorescence noise) and new phenol red-free medium (prewarmed to 37°C) was given to the cells (in case of glycocalyx-targeting enzymatic treatment containing again the enzymes). Then the plates were immediately transferred to the 3D-SIM Nikon A1 microscope (equipped with a stage-top incubation system (OkoLab), conditions: humid, 37°C, 5% CO_2) to take the images. An oil immersion 63x objective was used.
The thickness of the glycocalyx was determined from crops of the cell borders in the plane just above the cell/substrate interaction zone processed by means of ImageJ/FIJI[104] (for better distinction the "Enhance Contrast" tool was applied). The thickness measurements from the cropped images were then done with a customised macro in the MatLab environment that automatised the data collection after marking the thickness with lines. The graph was obtain with the help of Plotsofdata web apps[105].

4.6 Visualisation, recording and quantification of the actin dynamics

4.6.1 Transfection with LifeAct™ and recording

To visualise the actin dynamics, the PC12 cells were transfected with mCherry-LifeAct (the vector was a kind gift by Prof. Giorgio Scita). For this purpose, the cells were plated on Ø 35 mm petri dishes (TRP) at a low confluency (10-15%) the day before the transfection. At the beginning of the next day, the transfection was done with Lipofectamine LTX® performing the following steps:

- Solution 1: 6 µl of Lipofectamine LTX® was added to 150 µl RPMI base medium (incubation for 5 min at RT).
- Solution 2: 2 µl of the mCherry-LifeAct vector DNA (concentration 1 µg/µL) was added to 150 µl RPMI base medium, then 2 µl Plus™ reagent was added.
- The two solutions were mixed and incubated for 20 min at RT and then added dropwise to the cells in a homogeneous way.

The success of the transfection was controlled the next day with a Zeiss Axiovert 40 CFL with an epifluorescence module.
After transferring the transfected cells onto the indicated substrates (see 4.4), the actin dynamics (before and after glycocalyx removal, see 4.4) were then recorded the next day with a Nikon A1R confocal microscope at the UNI^TECH NOLIMITS Imaging facility of the University of Milan. The microscope is equipped with a stage-top incubation system (OkoLab) to guarantee humidification, 37°C and 5% CO_2 during the live

cell imaging. An oil immersion 60x objective was used. The recordings were done with a frame rate of 0.5 frames/sec for 2 minutes.

4.6.2 Analysis of the actin dynamics by Particle Image Velocimentry

Particle image velocimetry (PIV) was performed to quantify the actin dynamics. This analysis results in a vector field, highlighting the local movement of the actin fibres in time, from which the average flow speed can be obtained.

Pre-processing – For each movie, a 400 x 400 px (~ 20 x 20 µm) area was selected at the cell edge. Photobleaching was corrected in Fiji hypothesising linear decay of the signal and the cell area was segmented by thresholding. A temporal resolution of 6 s between frames was used (intermediate frames were removed).

Analysis – PIV analysis is described in detail elsewhere[106]. Briefly, a region of interest (source box) is searched for in a larger area (search box) of the subsequent frame by two-dimensional cross-correlation. A grid of regions of interest is drawn over the image, to obtain a full local tracking of the actin filaments. For this analysis, the PIV parameters were optimised as follows: source box 0.6 µm, search box 1 µm, distance between regions of interests (grid) 0.4 µm, correlation coefficient threshold of 0.3. Spatial and temporal convolutions are subsequently performed to interpolate the vector field. The defined kernels were 5 µm (sigma = 1 µm) and 30 s (sigma = 12 s), respectively. Colour maps display flow velocity within a 0-2 µm/min scale.

ACKNOWLEDGEMENTS

We acknowledge the support of the European Union's Horizon 2020 research and innovation programme under the Marie Skłodowska-Curie grant agreement No. 812772, project Phys2Biomed, and under FET Open grant agreement No. 801126, project EDIT. BS and SM are funded by the European Research Council (ERC) under the European Union's Horizon 2020 research and innovation programme (grant agreement No. 681808). PM and CS acknowledge support from the European Union FP7-NMP-2013-LARGE-7 "Future NanoNeeds" programme. CL gratefully acknowledges funding from Miur – PRIN2017, Prot. 2017YH9MRK.

We thank the UNI^{TECH} NOLIMITS Imaging facility of the University of Milan (in particular Dr. Miriam Ascagni) for support in regards to the realisation of the experiments involving confocal microscopy and 3D-SIM.

We thank Prof. Giorgio Scita, Prof. Jan de Boer, Prof. Johanna Ivaska, Dr. Martina Lerche and Aleksi Isomursu for critical reading of the drafts and valuable comments.

AUTHOR CONTRIBUTIONS

Conceptualisation: CS, AP; methodology – probe fabrication and characterisation: MC, APr, FB, CP; methodology – SCBD: APr, CP; methodology – cell culture and preparation: TD, MDU, CS; methodology – glycocalyx characterisation AFM: MC, LC, TD, CS, AP; methodology – AFM adhesion force spectroscopy: MC, TD, AP; methodology – actin dynamics: MDU, CS; methodology – glycocalyx characterisation 3D-SIM: MDU, CS; data curation and analysis – AFM glycocalyx characterisation: MC, LC, TD, CS, AP; data curation and analysis – AFM adhesion force spectroscopy: MC, TD, CS, AP; data curation and analysis – actin dynamics: MDU, SM, BS, CS; data curation and analysis - glycocalyx characterisation 3D-SIM: CF, CS; original draft writing: MC, CS; draft reviewing and editing: MC, TD, CL, PM, SM, BS, AP, CS; supervision: CL, PM, BS, CS, AP; resources, funding and project administration: CL, PM, BS, AP. Author contributions were allocated adopting the terminology of CRediT – Contributor Roles Taxonomy.

REFERENCES

1. Gauthier, N. C. & Roca-Cusachs, P. Mechanosensing at integrin-mediated cell–matrix adhesions: from molecular to integrated mechanisms. *Current Opinion in Cell Biology* **50**, 20–26 (2018).
2. Kechagia, J. Z., Ivaska, J. & Roca-Cusachs, P. Integrins as biomechanical sensors of the microenvironment. *Nature Reviews Molecular Cell Biology* 1 (2019) doi:10.1038/s41580-019-0134-2.
3. Jansen, K. A. *et al.* A guide to mechanobiology: Where biology and physics meet. *Biochimica et Biophysica Acta (BBA) - Molecular Cell Research* **1853**, 3043–3052 (2015).
4. Di Cio, S. & Gautrot, J. E. Cell sensing of physical properties at the nanoscale: Mechanisms and control of cell adhesion and phenotype. *Acta Biomaterialia* **30**, 26–48 (2016).
5. Sun, Z., Costell, M. & Fässler, R. Integrin activation by talin, kindlin and mechanical forces. *Nature Cell Biology* **21**, 25 (2019).
6. Chighizola, M. *et al.* Mechanotransduction in neuronal cell development and functioning. *Biophys Rev* (2019) doi:10.1007/s12551-019-00587-2.
7. Dalby, M. J., Gadegaard, N. & Oreffo, R. O. C. Harnessing nanotopography and integrin-matrix interactions to influence stem cell fate. *Nat Mater* **13**, 558–569 (2014).
8. Chen, W., Shao, Y., Li, X., Zhao, G. & Fu, J. Nanotopographical Surfaces for Stem Cell Fate Control: Engineering Mechanobiology from the Bottom. *Nano Today* **9**, 759–784 (2014).
9. Schulte, C. *et al.* Conversion of nanoscale topographical information of cluster-assembled zirconia surfaces into mechanotransductive events promotes neuronal differentiation. *Journal of Nanobiotechnology* **14**, 18 (2016).
10. Maffioli, E. *et al.* Proteomic dissection of nanotopography-sensitive mechanotransductive signalling hubs that foster neuronal differentiation in PC12 cells. *Front. Cell. Neurosci.* **11**, (2017).
11. Chen, W. *et al.* Nanotopography Regulates Motor Neuron Differentiation of Human Pluripotent Stem Cells. *Nanoscale* (2018) doi:10.1039/C7NR05430K.
12. Baek, J. *et al.* Distinct Mechanosensing of Human Neural Stem Cells on Extremely Limited Anisotropic Cellular Contact. *ACS Appl Mater Interfaces* (2018) doi:10.1021/acsami.8b10171.
13. Galli, A. *et al.* Cluster-assembled zirconia substrates promote long-term differentiation and functioning of human islets of Langerhans. *Sci Rep* **8**, 9979 (2018).
14. Gasiorowski, J. Z., Murphy, C. J. & Nealey, P. F. Biophysical cues and cell behavior: the big impact of little things. *Annu Rev Biomed Eng* **15**, 155–176 (2013).
15. Young, J. L., Holle, A. W. & Spatz, J. P. Nanoscale and mechanical properties of the physiological cell–ECM microenvironment. *Experimental Cell Research* **343**, 3–6 (2016).
16. Leclech, C., Natale, C. F. & Barakat, A. I. The basement membrane as a structured surface – role in vascular health and disease. *J Cell Sci* **133**, (2020).
17. Park, J. *et al.* Directed migration of cancer cells guided by the graded texture of the underlying matrix. *Nat Mater* **15**, 792–801 (2016).
18. Park, J., Kim, D.-H. & Levchenko, A. Topotaxis: A New Mechanism of Directed Cell Migration in Topographic ECM Gradients. *Biophys. J.* **114**, 1257–1263 (2018).
19. Chighizola, M. *et al.* Adhesion force spectroscopy with nanostructured colloidal probes reveals nanotopography-dependent early mechanotransductive interactions at the cell membrane level. *Nanoscale* (2020) doi:10.1039/D0NR01991G.
20. Sun, Z., Guo, S. S. & Fässler, R. Integrin-mediated mechanotransduction. *J Cell Biol* jcb.201609037 (2016) doi:10.1083/jcb.201609037.
21. Paszek, M. J. *et al.* The cancer glycocalyx mechanically primes integrin-mediated growth and survival. *Nature* **511**, 319–325 (2014).
22. Kuo, J. C.-H., Gandhi, J. G., Zia, R. N. & Paszek, M. J. Physical biology of the cancer cell glycocalyx. *Nature Physics* **14**, 658–669 (2018).
23. Marsico, G., Russo, L., Quondamatteo, F. & Pandit, A. Glycosylation and Integrin Regulation in Cancer. *Trends in Cancer* **4**, 537–552 (2018).
24. Buffone, A. & Weaver, V. M. Don't sugarcoat it: How glycocalyx composition influences cancer progression. *J Cell Biol* **219**, (2020).
25. Wegner, K., Piseri, P., Tafreshi, H. V. & Milani, P. Cluster beam deposition: a tool for nanoscale science and technology. *J. Phys. D: Appl. Phys.* **39**, R439 (2006).
26. Schulte, C., Podestà, A., Lenardi, C., Tedeschi, G. & Milani, P. Quantitative Control of Protein and Cell Interaction with Nanostructured Surfaces by Cluster Assembling. *Acc. Chem. Res.* **50**, 231–239 (2017).
27. Schulte, C. *et al.* Scale Invariant Disordered Nanotopography Promotes Hippocampal Neuron Development and Maturation with Involvement of Mechanotransductive Pathways. *Front Cell Neurosci* **10**, 267 (2016).

28. Alessandra, G. *et al.* Shaping Pancreatic β-Cell Differentiation and Functioning: The Influence of Mechanotransduction. *Cells* **9**, 413 (2020).
29. Schulte, C. 10 - Cluster-assembled nanostructured materials for cell biology. in *Frontiers of Nanoscience* (eds. Milani, P. & Sowwan, M.) vol. 15 271–289 (Elsevier, 2020).
30. Maffioli, E. *et al.* Proteomic Analysis Reveals a Mitochondrial Remodeling of βTC3 Cells in Response to Nanotopography. *Front. Cell Dev. Biol.* **8**, (2020).
31. Sokolov, I., Iyer, S., Subba-Rao, V., Gaikwad, R. M. & Woodworth, C. D. Detection of surface brush on biological cells in vitro with atomic force microscopy. *Appl. Phys. Lett.* **91**, 023902 (2007).
32. Iyer, S., Gaikwad, R. M., Subba-Rao, V., Woodworth, C. D. & Sokolov, I. AFM Detects Differences in the Surface Brush of Normal and Cancerous Cervical Cells. *Nat Nanotechnol* **4**, 389–393 (2009).
33. Sokolov, I., Dokukin, M. E. & Guz, N. V. Method for quantitative measurements of the elastic modulus of biological cells in AFM indentation experiments. *Methods* **60**, 202–213 (2013).
34. Kirfel, G., Rigort, A., Borm, B., Schulte, C. & Herzog, V. Structural and compositional analysis of the keratinocyte migration track. *Cell Motility* **55**, 1–13 (2003).
35. Kirfel, G., Rigort, A., Borm, B. & Herzog, V. Cell migration: mechanisms of rear detachment and the formation of migration tracks. *European Journal of Cell Biology* **83**, 717–724 (2004).
36. Ma, L. *et al.* Discovery of the migrasome, an organelle mediating release of cytoplasmic contents during cell migration. *Cell Research* **25**, 24–38 (2015).
37. Abrams, G. A., Goodman, S. L., Nealey, P. F., Franco, M. & Murphy, C. J. Nanoscale topography of the basement membrane underlying the corneal epithelium of the rhesus macaque. *Cell Tissue Res.* **299**, 39–46 (2000).
38. Vicente-Manzanares, M. & Horwitz, A. R. Adhesion dynamics at a glance. *J Cell Sci* **124**, 3923–3927 (2011).
39. Changede, R. & Sheetz, M. Integrin and cadherin clusters: A robust way to organize adhesions for cell mechanics. *BioEssays* **39**, n/a-n/a (2017).
40. Li, F., Redick, S. D., Erickson, H. P. & Moy, V. T. Force measurements of the alpha5beta1 integrin-fibronectin interaction. *Biophys. J.* **84**, 1252–1262 (2003).
41. Taubenberger, A. *et al.* Revealing Early Steps of α2β1 Integrin-mediated Adhesion to Collagen Type I by Using Single-Cell Force Spectroscopy. *Mol Biol Cell* **18**, 1634–1644 (2007).
42. Dufrêne, Y. F. *et al.* Five challenges to bringing single-molecule force spectroscopy into living cells. *Nat. Methods* **8**, 123–127 (2011).
43. Strohmeyer, N., Bharadwaj, M., Costell, M., Fässler, R. & Müller, D. J. Fibronectin-bound α5β1 integrins sense load and signal to reinforce adhesion in less than a second. *Nat Mater* **16**, 1262–1270 (2017).
44. Evans, E. A. & Calderwood, D. A. Forces and bond dynamics in cell adhesion. *Science* **316**, 1148–1153 (2007).
45. Mescola, A. *et al.* Probing cytoskeleton organisation of neuroblastoma cells with single-cell force spectroscopy. *J. Mol. Recognit.* **25**, 270–277 (2012).
46. Elosegui-Artola, A. *et al.* Mechanical regulation of a molecular clutch defines force transmission and transduction in response to matrix rigidity. *Nature Cell Biology* **18**, 540–548 (2016).
47. Oria, R. *et al.* Force loading explains spatial sensing of ligands by cells. *Nature* **552**, 219 (2017).
48. Case, L. B. & Waterman, C. M. Integration of actin dynamics and cell adhesion by a three-dimensional, mechanosensitive molecular clutch. *Nat. Cell Biol.* **17**, 955–963 (2015).
49. Gardel, M. L. *et al.* Traction stress in focal adhesions correlates biphasically with actin retrograde flow speed. *J. Cell Biol.* **183**, 999–1005 (2008).
50. Alexandrova, A. Y. *et al.* Comparative Dynamics of Retrograde Actin Flow and Focal Adhesions: Formation of Nascent Adhesions Triggers Transition from Fast to Slow Flow. *PLoS One* **3**, (2008).
51. Renkawitz, J. *et al.* Adaptive force transmission in amoeboid cell migration. *Nat. Cell Biol.* **11**, 1438–1443 (2009).
52. Schulte, C. *et al.* Lamellipodial tension, not integrin/ligand binding, is the crucial factor to realise integrin activation and cell migration. *Eur. J. Cell Biol.* **95**, 1–14 (2016).
53. Nichol, R. H., Hagen, K. M., Lumbard, D. C., Dent, E. W. & Gómez, T. M. Guidance of Axons by Local Coupling of Retrograde Flow to Point Contact Adhesions. *J. Neurosci.* **36**, 2267–2282 (2016).
54. Stricker, J., Aratyn-Schaus, Y., Oakes, P. W. & Gardel, M. L. Spatiotemporal Constraints on the Force-Dependent Growth of Focal Adhesions. *Biophysical Journal* **100**, 2883–2893 (2011).
55. Choi, C. K. *et al.* Actin and alpha-actinin orchestrate the assembly and maturation of nascent adhesions in a myosin II motor-independent manner. *Nat. Cell Biol.* **10**, 1039–1050 (2008).
56. Changede, R., Xu, X., Margadant, F. & Sheetz, M. P. Nascent Integrin Adhesions Form on All Matrix Rigidities after Integrin Activation. *Dev. Cell* **35**, 614–621 (2015).
57. Schvartzman, M. *et al.* Nanolithographic Control of the Spatial Organization of Cellular Adhesion Receptors at the Single-Molecule Level. *Nano Lett.* **11**, 1306–1312 (2011).
58. Coyer, S. R. *et al.* Nanopatterning reveals an ECM area threshold for focal adhesion assembly and force transmission that is regulated by integrin activation and cytoskeleton tension. *J Cell Sci* **125**, 5110–5123 (2012).

59. Malmström, J. *et al.* Large Area Protein Patterning Reveals Nanoscale Control of Focal Adhesion Development. *Nano Lett.* **10**, 686–694 (2010).
60. Changede, R., Cai, H., Wind, S. J. & Sheetz, M. P. Integrin nanoclusters can bridge thin matrix fibres to form cell–matrix adhesions. *Nat. Mater.* 1–10 (2019) doi:10.1038/s41563-019-0460-y.
61. Arnold, M. *et al.* Activation of integrin function by nanopatterned adhesive interfaces. *Chemphyschem* **5**, 383–388 (2004).
62. Cavalcanti-Adam, E. A. *et al.* Cell Spreading and Focal Adhesion Dynamics Are Regulated by Spacing of Integrin Ligands. *Biophysical Journal* **92**, 2964–2974 (2007).
63. Liu, Y. *et al.* Nanoparticle tension probes patterned at the nanoscale: impact of integrin clustering on force transmission. *Nano Lett.* **14**, 5539–5546 (2014).
64. Huang, J. *et al.* Impact of order and disorder in RGD nanopatterns on cell adhesion. *Nano Lett.* **9**, 1111–1116 (2009).
65. Di Cio, S., Iskratsch, T., Connelly, J. T. & Gautrot, J. E. Contractile myosin rings and cofilin-mediated actin disassembly orchestrate ECM nanotopography sensing. *Biomaterials* **232**, 119683 (2020).
66. Wolfenson, H. *et al.* Tropomyosin controls sarcomere-like contractions for rigidity sensing and suppressing growth on soft matrices. *Nature Cell Biology* **18**, 33–42 (2016).
67. Sheetz, M. A Tale of Two States: Normal and Transformed, With and Without Rigidity Sensing. *Annual Review of Cell and Developmental Biology* **35**, 169–190 (2019).
68. Feld, L. *et al.* Cellular contractile forces are nonmechanosensitive. *Science Advances* **6**, eaaz6997 (2020).
69. Chaudhuri, P. K., Low, B. C. & Lim, C. T. Mechanobiology of Tumor Growth. *Chem. Rev.* **118**, 6499–6515 (2018).
70. Lee, G., Han, S.-B., Lee, J.-H., Kim, H.-W. & Kim, D.-H. Cancer Mechanobiology: Microenvironmental Sensing and Metastasis. *ACS Biomater. Sci. Eng.* (2019) doi:10.1021/acsbiomaterials.8b01230.
71. Yang, B. *et al.* Stopping transformed cancer cell growth by rigidity sensing. *Nature Materials* **19**, 239–250 (2020).
72. Ingber, D. Mechanobiology and diseases of mechanotransduction. *Annals of Medicine* **35**, 564–577 (2003).
73. Hamidi, H. & Ivaska, J. Every step of the way: integrins in cancer progression and metastasis. *Nat. Rev. Cancer* **18**, 533–548 (2018).
74. Papalazarou, V., Salmeron-Sanchez, M. & Machesky, L. M. Tissue engineering the cancer microenvironment—challenges and opportunities. *Biophys Rev* **10**, 1695–1711 (2018).
75. Nebuloni, M. *et al.* Insight On Colorectal Carcinoma Infiltration by Studying Perilesional Extracellular Matrix. *Sci Rep* **6**, 22522 (2016).
76. Bonnans, C., Chou, J. & Werb, Z. Remodelling the extracellular matrix in development and disease. *Nat Rev Mol Cell Biol* **15**, 786–801 (2014).
77. Cox, T. R. The matrix in cancer. *Nature Reviews Cancer* 1–22 (2021) doi:10.1038/s41568-020-00329-7.
78. Tarbell, J. M. & Cancel, L. M. The glycocalyx and its significance in human medicine. *Journal of Internal Medicine* **280**, 97–113 (2016).
79. Winograd-Katz, S. E., Fässler, R., Geiger, B. & Legate, K. R. The integrin adhesome: from genes and proteins to human disease. *Nat. Rev. Mol. Cell Biol.* **15**, 273–288 (2014).
80. Wolfenson, H., Yang, B. & Sheetz, M. P. Steps in Mechanotransduction Pathways that Control Cell Morphology. *Annu. Rev. Physiol.* **81**, 585–605 (2019).
81. Barnes, J. M. *et al.* A tension-mediated glycocalyx–integrin feedback loop promotes mesenchymal-like glioblastoma. *Nature Cell Biology* **20**, 1203 (2018).
82. Chronopoulos, A. *et al.* Syndecan-4 tunes cell mechanics by activating the kindlin-integrin-RhoA pathway. *Nature Materials* **19**, 669–678 (2020).
83. Miyata, S. & Kitagawa, H. Formation and remodeling of the brain extracellular matrix in neural plasticity: Roles of chondroitin sulfate and hyaluronan. *Biochim Biophys Acta Gen Subj* **1861**, 2420–2434 (2017).
84. Freeman, S. A. *et al.* Transmembrane Pickets Connect Cyto- and Pericellular Skeletons Forming Barriers to Receptor Engagement. *Cell* **172**, 305-317.e10 (2018).
85. Ferraris, G. M. S. *et al.* The interaction between uPAR and vitronectin triggers ligand-independent adhesion signalling by integrins. *EMBO J.* **33**, 2458–2472 (2014).
86. Lou, H.-Y. *et al.* Membrane curvature underlies actin reorganization in response to nanoscale surface topography. *Proc. Natl. Acad. Sci. U.S.A.* **116**, 23143–23151 (2019).
87. Sheridan, C. Pancreatic cancer provides testbed for first mechanotherapeutics. *Nature Biotechnology* **37**, 829–831 (2019).
88. Cully, M. Integrin-targeted therapies branch out. *Nature Reviews Drug Discovery* (2020) doi:10.1038/d41573-020-00180-3.
89. Indrieri, M., Podestà, A., Bongiorno, G., Marchesi, D. & Milani, P. Adhesive-free colloidal probes for nanoscale force measurements: Production and characterization. *Review of Scientific Instruments* **82**, 023708 (2011).

90. Chighizola, M., Puricelli, L., Bellon, L. & Podestà, A. Large colloidal probes for atomic force microscopy: Fabrication and calibration issues. *Journal of Molecular Recognition* **34**, e2879 (2021).
91. Hutter, J. L. & Bechhoefer, J. Calibration of atomic-force microscope tips. *Review of Scientific Instruments* **64**, 1868–1873 (1993).
92. Butt, H.-J. & Jaschke, M. Calculation of thermal noise in atomic force microscopy. *Nanotechnology* **6**, 1 (1995).
93. Laurent, J., Steinberger, A. & Bellon, L. Functionalized AFM probes for force spectroscopy: eigenmode shapes and stiffness calibration through thermal noise measurements. *Nanotechnology* **24**, 225504 (2013).
94. Barborini, E., Piseri, P. & Milani, P. A pulsed microplasma source of high intensity supersonic carbon cluster beams. *J. Phys. D: Appl. Phys.* **32**, L105–L109 (1999).
95. Tafreshi, H. V., Piseri, P., Benedek, G. & Milani, P. The role of gas dynamics in operation conditions of a Pulsed Microplasma Cluster Source for nanostructured thin films deposition. *J Nanosci Nanotechnol* **6**, 1140–1149 (2006).
96. Podestà, A. *et al.* Nanomanufacturing of titania interfaces with controlled structural and functional properties by supersonic cluster beam deposition. *Journal of Applied Physics* **118**, 234309 (2015).
97. Borghi, F., Podestà, A., Piazzoni, C. & Milani, P. Growth Mechanism of Cluster-Assembled Surfaces: From Submonolayer to Thin-Film Regime. *Phys. Rev. Applied* **9**, 044016 (2018).
98. Borghi, F. *et al.* Cluster-assembled cubic zirconia films with tunable and stable nanoscale morphology against thermal annealing. *Journal of Applied Physics* **120**, 055302 (2016).
99. Borghi, F., Scaparra, B., Paternoster, C., Milani, P. & Podestà, A. Electrostatic Double-Layer Interaction at the Surface of Rough Cluster-Assembled Films: The Case of Nanostructured Zirconia. *Langmuir* **34**, 10230–10242 (2018).
100. Schillers, H. *et al.* Standardized Nanomechanical Atomic Force Microscopy Procedure (SNAP) for Measuring Soft and Biological Samples. *Scientific Reports* **7**, 5117 (2017).
101. Janovjak, H., Struckmeier, J. & Müller, D. J. Hydrodynamic effects in fast AFM single-molecule force measurements. *Eur. Biophys. J.* **34**, 91–96 (2005).
102. Puricelli, L., Galluzzi, M., Schulte, C., Podestà, A. & Milani, P. Nanomechanical and topographical imaging of living cells by atomic force microscopy with colloidal probes. *Rev Sci Instrum* **86**, 033705 (2015).
103. Zeng, Y., Ebong, E. E., Fu, B. M. & Tarbell, J. M. The Structural Stability of the Endothelial Glycocalyx after Enzymatic Removal of Glycosaminoglycans. *PLOS ONE* **7**, e43168 (2012).
104. Schindelin, J. *et al.* Fiji: an open-source platform for biological-image analysis. *Nature Methods* **9**, 676–682 (2012).
105. Postma, M. & Goedhart, J. PlotsOfData—A web app for visualizing data together with their summaries. *PLOS Biology* **17**, e3000202 (2019).
106. Yolland, L. *et al.* Persistent and polarized global actin flow is essential for directionality during cell migration. *Nat. Cell Biol.* **21**, 1370–1381 (2019).

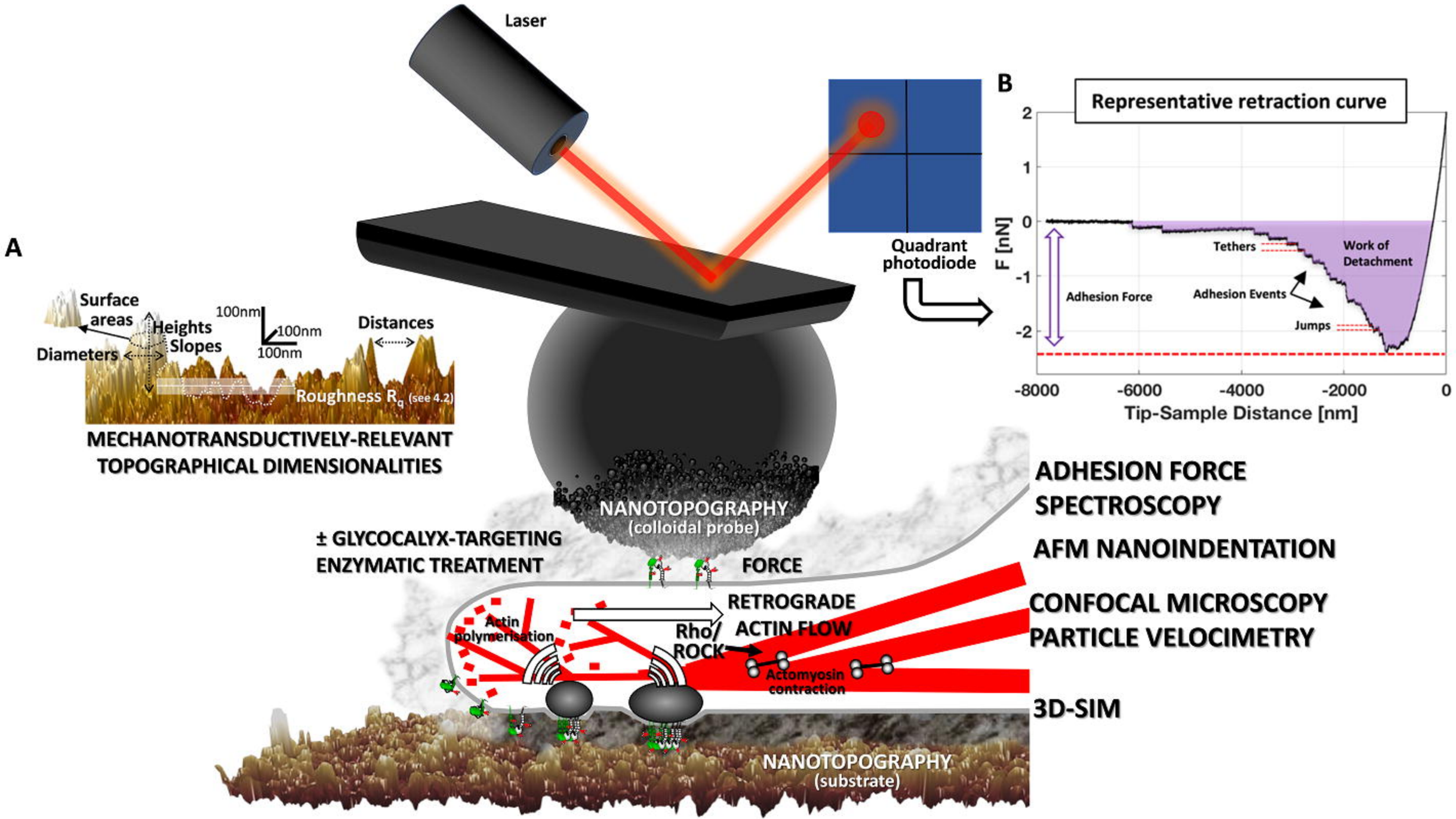
A
Laser
Quadrant photodiode
B
Representative retraction curve
F [nN]
Tip-Sample Distance [nm]
Tethers
Work of Detachment
Adhesion Force
Adhesion Events
Jumps
Surface areas
Heights
Slopes
Diameters
100nm
100nm
100nm
Distances
Roughness R_q (see 4.2)
MECHANOTRANSDUCTIVELY-RELEVANT TOPOGRAPHICAL DIMENSIONALITIES
NANOTOPOGRAPHY (colloidal probe)
± GLYCOCALYX-TARGETING ENZYMATIC TREATMENT
FORCE
RETROGRADE ACTIN FLOW
Actin polymerisation
Rho/ ROCK
Actomyosin contraction
NANOTOPOGRAPHY (substrate)
ADHESION FORCE SPECTROSCOPY
AFM NANOINDENTATION
CONFOCAL MICROSCOPY
PARTICLE VELOCIMETRY
3D-SIM

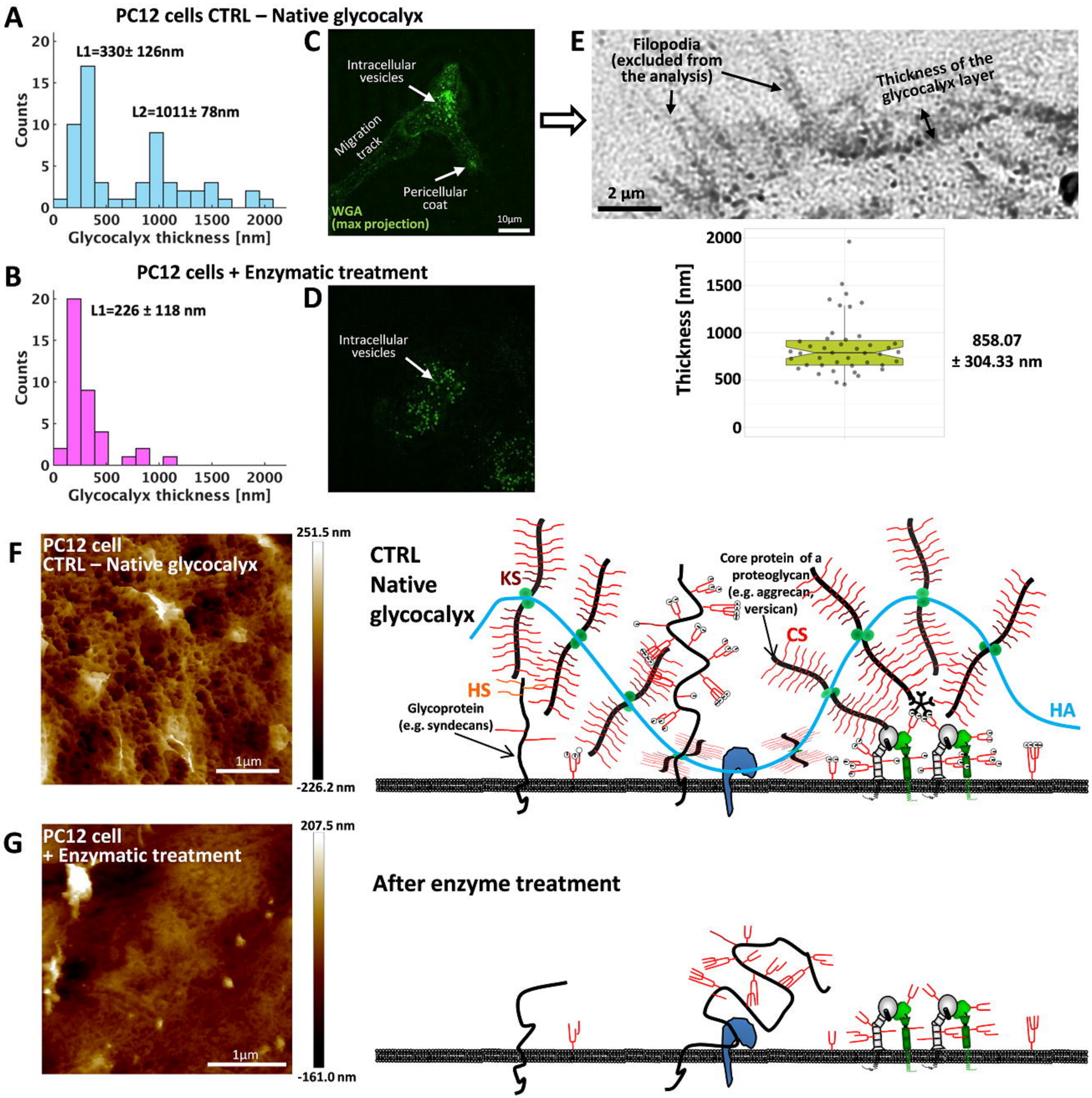
A
PC12 cells CTRL – Native glycocalyx
L1=330± 126nm
L2=1011± 78nm
Counts
Glycocalyx thickness [nm]
B
PC12 cells + Enzymatic treatment
L1=226 ± 118 nm
Counts
Glycocalyx thickness [nm]
C
Intracellular vesicles
Migration track
Pericellular coat
WGA (max projection)
10µm
D
Intracellular vesicles
E
Filopodia (excluded from the analysis)
Thickness of the glycocalyx layer
2 µm
Thickness [nm]
858.07 ± 304.33 nm
F
PC12 cell
CTRL – Native glycocalyx
251.5 nm
-226.2 nm
1µm
G
PC12 cell
+ Enzymatic treatment
207.5 nm
-161.0 nm
1µm
CTRL Native glycocalyx
KS
HS
Glycoprotein (e.g. syndecans)
Core protein of a proteoglycan (e.g. aggrecan, versican)
CS
HA
After enzyme treatment

A CTRL — — — Enzymatic treatment

Adhesion force F_a

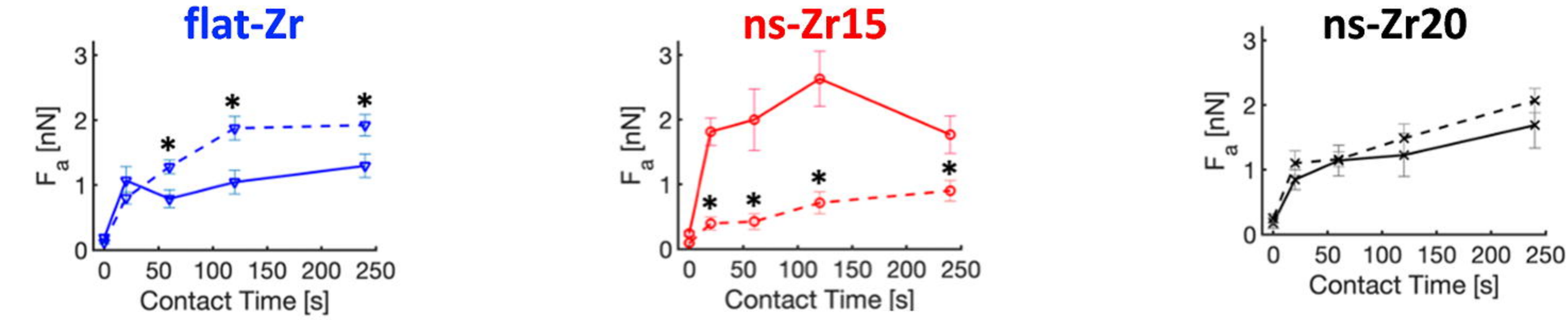

B

Number of jump adhesive events N_j

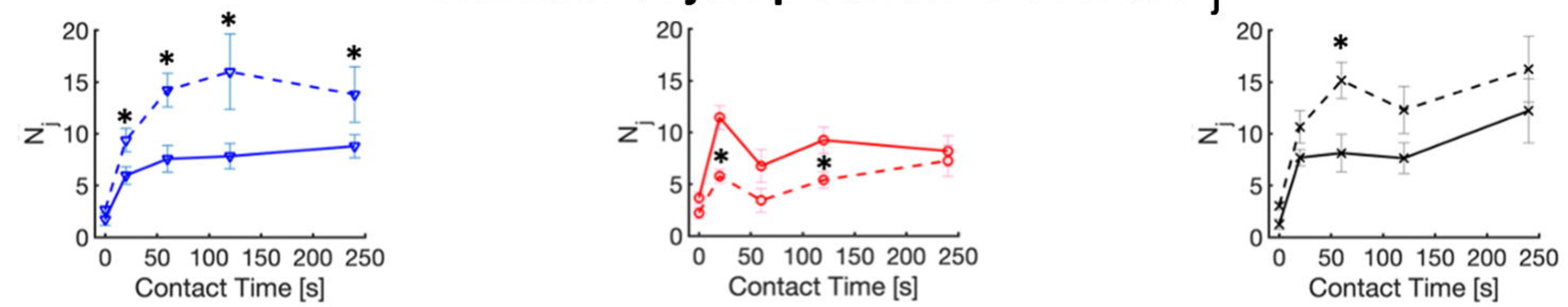

C

Mean jump force $\langle F_j \rangle$

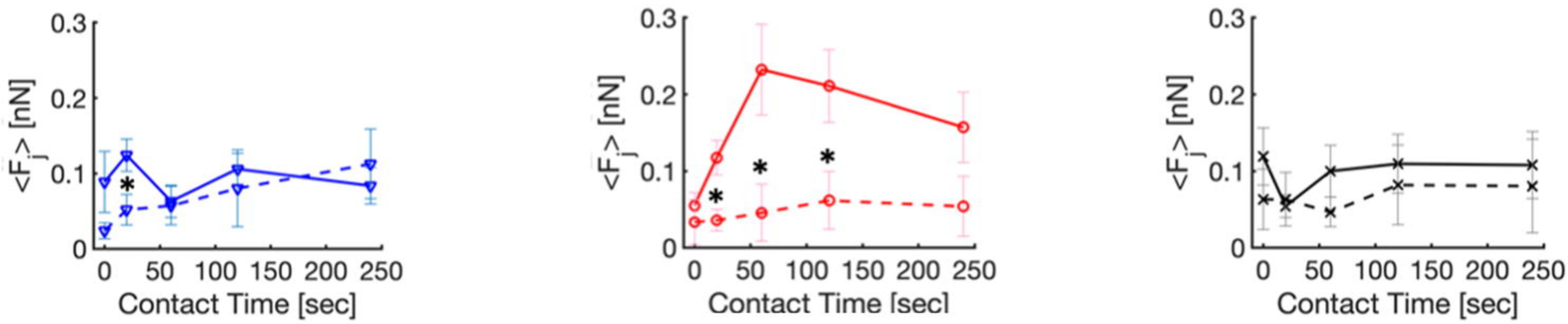

D

Jump force distribution

CTRL

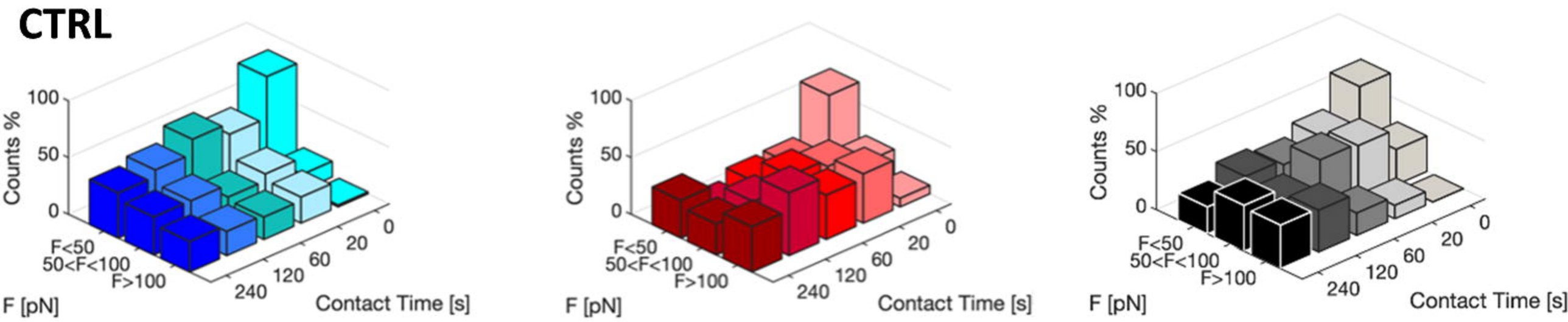

Enzymatic treatment

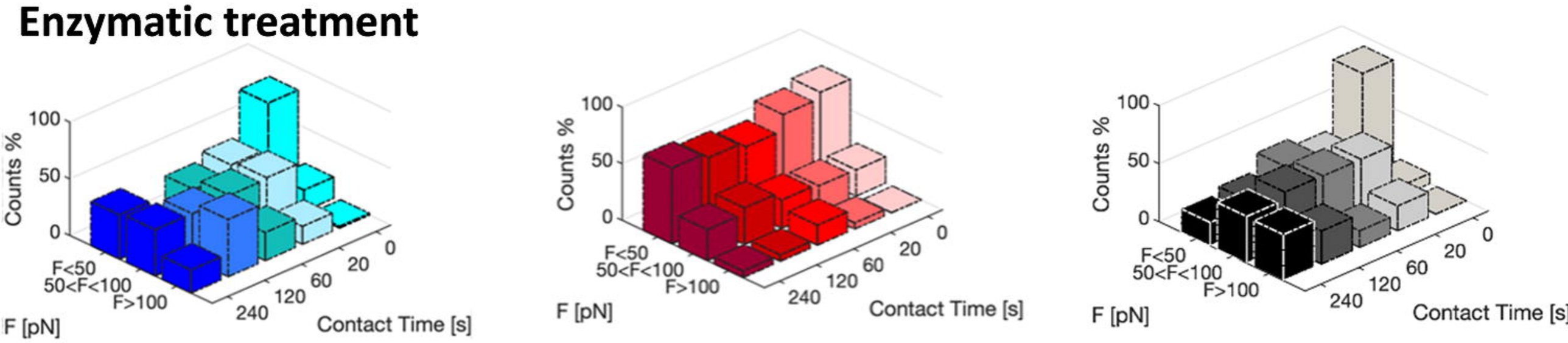

E

Table 1 – Most probable jump forces at 0 s

Topography/experimental condition	CTRL	Enzymatic treatment
flat-Zr	44 ± 16 pN	25 ± 18 pN
ns-Zr15	39 ± 16 pN	28 ± 10 pN
ns-Zr20	43 ± 17 pN	33 ± 11 pN

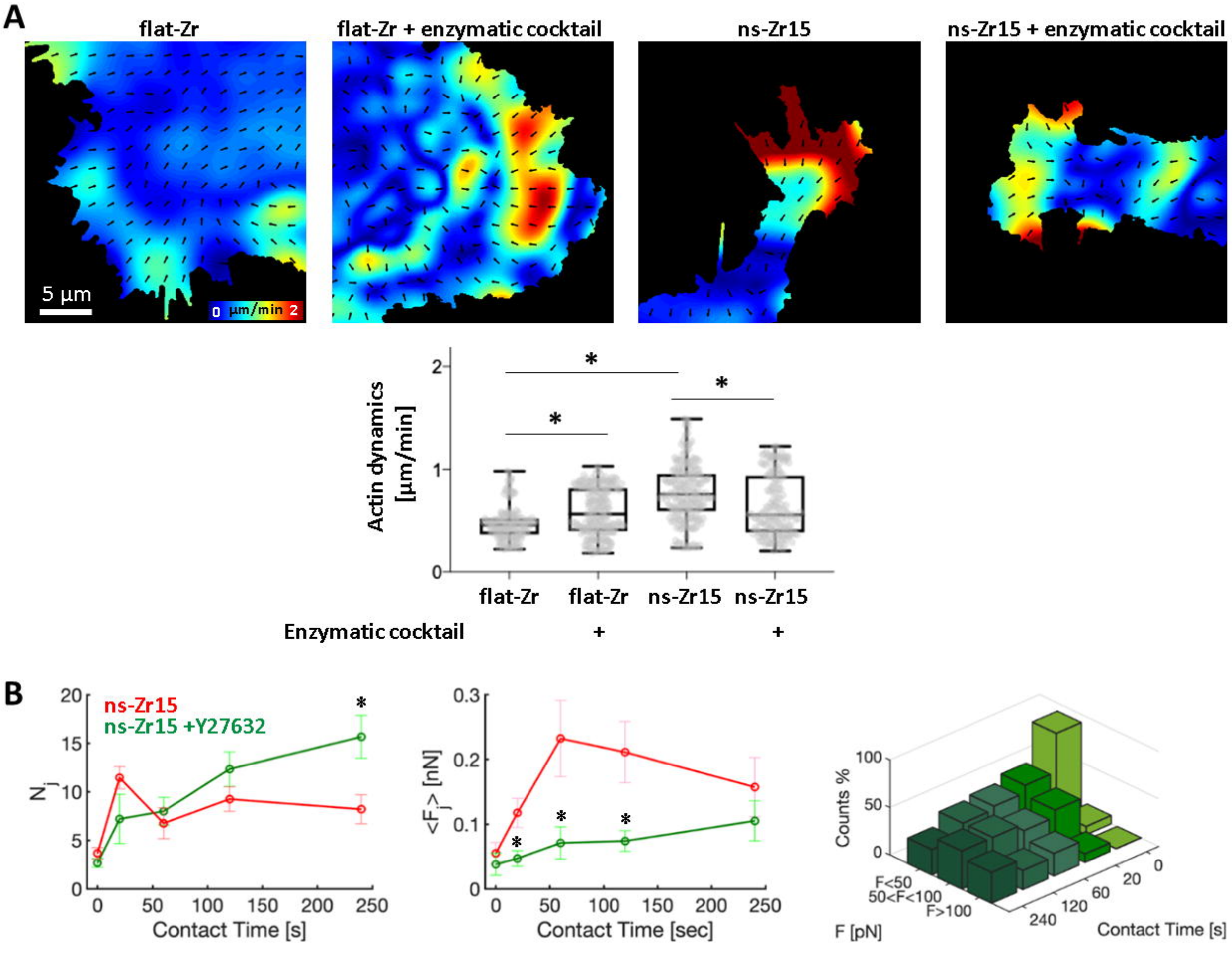
A
flat-Zr
flat-Zr + enzymatic cocktail
ns-Zr15
ns-Zr15 + enzymatic cocktail
5 µm
0 µm/min 2
Actin dynamics [µm/min]
flat-Zr
flat-Zr
ns-Zr15
ns-Zr15
Enzymatic cocktail
+
+
B
ns-Zr15
ns-Zr15 +Y27632
Contact Time [s]
Contact Time [sec]
Counts %
F [pN]
F<50
50<F<100
F>100
Contact Time [s]

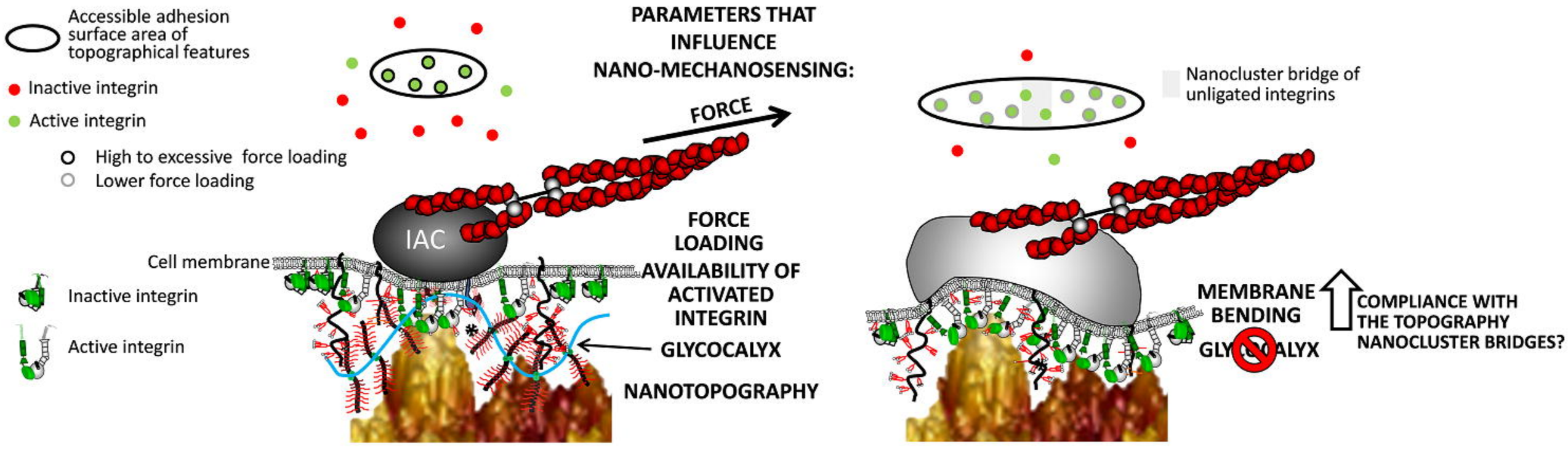
Accessible adhesion surface area of topographical features
Inactive integrin
Active integrin
High to excessive force loading
Lower force loading
PARAMETERS THAT INFLUENCE NANO-MECHANOSENSING:
FORCE
IAC
Cell membrane
Inactive integrin
Active integrin
FORCE LOADING
AVAILABILITY OF ACTIVATED INTEGRIN
GLYCOCALYX
NANOTOPOGRAPHY
Nanocluster bridge of unligated integrins
MEMBRANE BENDING
COMPLIANCE WITH THE TOPOGRAPHY NANOCLUSTER BRIDGES?